The Astrophysical Journal, 974:150 (18pp), 2024 October 20 https://doi.org/10.3847/1538-4357/ad7026

Accretion and Outflow in Orion-KL Source I

Melvyn Wright[1], Brett A. McGuire[2,3], Adam Ginsburg[4], Tomoya Hirota[5,6], John Bally[7], Ryan Hwangbo[1], T. Dex Bhadra[1], Chris John[1,8], and Rishabh Dave[1]
[1] Department of Astronomy, University of California, 501 Campbell Hall, Berkeley, CA 94720-3441, USA; melvyn@berkeley.edu
[2] Department of Chemistry, Massachusetts Institute of Technology, Cambridge, MA 02139, USA
[3] National Radio Astronomy Observatory, Charlottesville, VA 22903, USA
[4] Department of Astronomy, University of Florida, 211 Bryant Space Science Center P.O. Box 112055, Gainesville, FL 32611-2055, USA
[5] Mizusawa VLBI Observatory, National Astronomical Observatory of Japan, 2-12, Hoshigaoka, Mizusawa, Oshu, Iwate 023-0861, Japan
[6] The Graduate University for Advanced Studies, SOKENDAI, 2-21-1 Osawa, Mitaka, Tokyo 181-8588, Japan
[7] CASA, University of Colorado, 389-UCB, Boulder, CO 80309, USA
[8] Troy High School, 2200 Dorothy Lane, Fullerton, CA 92831, USA
Received 2024 July 1; revised 2024 August 7; accepted 2024 August 7; published 2024 October 10

Abstract

We present Atacama Large Millimeter/submillimeter Array observations of SiO, SiS, H_2O, NaCl, and SO line emission at ∼30–50 mas resolution. These images map the molecular outflow and disk of Orion Source I (SrcI) on ∼12–20 au scales. Our observations show that the flow of material around SrcI creates a turbulent boundary layer in the outflow from SrcI, which may dissipate angular momentum in the rotating molecular outflow into the surrounding medium. Additionally, the data suggest that the proper motion of SrcI may have a significant effect on the structure and evolution of SrcI and its molecular outflow. As the motion of SrcI funnels material between the disk and the outflow, some material may be entrained into the outflow and accrete onto the disk, creating shocks that excite the NaCl close to the disk surface.

Unified Astronomy Thesaurus concepts: Protostars (1302); Circumstellar disks (235); Molecular gas (1073); Astrochemistry (75)

1. Introduction

Massive stars play an important role in numerous astrophysical processes, but their formation and evolution remain ambiguous. Current theory regarding high-mass ($>8M_\odot$) protostellar evolution strongly suggests that accretion onto the central parts via disks, and the specific geometry and rate are key variables that dictate the characteristics of the resulting star (T. Hosokawa et al. 2010; A. Caratti o Garatti et al. 2017). Efforts to find a mechanism that reconciles the infalling accreted material and outgoing outflows/radiation have resulted in numerous theories regarding the necessary rate and three-dimensional accretion flow geometry (e.g., T. Hosokawa et al. 2010; R. Kuiper et al. 2011; B. A. Whitney et al. 2013). Other theories, such as stellar mergers (I. A. Bonnell et al. 1998) and competitive accretion (I. A. Bonnell 2008) have also been considered. However, regardless of the specifics, the mechanism must be able to move material into the protostar for it to continue growing.

A study of the evolution of high-mass protostars is possible in the Kleinmann–Low Nebula in Orion (Orion-KL). At a distance of 415 pc (K. M. Menten et al. 2007; M. K. Kim et al. 2008; M. Kounkel et al. 2018), Orion-KL is the nearest interstellar cloud with observable massive star formation.

Observations of Orion-KL and simulations suggest that three stars were involved in a dynamical decay event approximately 550 yr ago, which ejected them from a multistar system (J. Bally et al. 2017, 2020). One of these stars, the Becklin–Neugebauer (BN) object, has a proper motion of $\sim 26\,\mathrm{km\,s^{-1}}$ northwestward. Radio Source I (SrcI) is another star involved and moves at $\sim 10\,\mathrm{km\,s^{-1}}$ southward. Finally, near-infrared source x (SrcX) moves at $\sim 55\,\mathrm{km\,s^{-1}}$ southeastward (K. L. Luhman et al. 2017; L. F. Rodríguez et al. 2017; S. A. Dzib et al. 2017). Direct observation of the central object in SrcI is not possible as the high opacity of the continuum emission from the SrcI disk conceals the central source. The specific nature and mass of this object have been the subject of extensive study and theorization. Estimation through conservation of linear momentum and dynamical simulation best agreed with SrcI being a $\sim 20M_\odot$ binary (proto)star system (C. Goddi et al. 2011a; L. F. Rodríguez et al. 2017, 2020; J. Bally et al. 2020). A. Ginsburg et al. (2018) found SrcI to have a mass of $15 \pm 2M_\odot$ by fitting the rotation curve of the H_2O $5_{5,0} - 6_{4,3}$ spectral line.

To build stronger constraints on its nature, we explore the outflow SrcI produces due to its close association with accretion. Outflows provide an avenue to carry excess angular momentum out of the system, enabling accreting matter to fall upon the star. This transfer of momentum and kinetic energy influences star formation in surrounding regions.

SrcI has been well studied as it is the closest observable high-mass protostar with a circumstellar disk and molecular outflow (T. Hirota et al. 2014; R. L. Plambeck & M. C. H. Wright 2016; A. Ginsburg et al. 2018). The molecular outflow from SrcI is prominent in SiO, SO, and SiS (J. A. López-Vázquez et al. 2020; M. Wright et al. 2020; T. Hirota et al. 2020). The disk and outflow are associated with SiO and H_2O masers (M. J. Reid et al. 2007; C. Goddi et al. 2009, 2011b; R. L. Plambeck et al. 2009; L. D. Matthews et al. 2010; F. Niederhofer et al. 2012; L. J. Greenhill et al. 2013). The mechanisms that drive outflows, such as the entrainment of molecular gas by a higher-velocity jet or an MHD-driven outflow by magneto-centrifugal disk winds, are still poorly understood (B. Commerçon et al. 2022).

In this paper, we reexamine our observational data from the Atacama Large Millimeter/submillimeter Array (ALMA),

Table 1
Observations

Freq (GHz)	Project Code	Date	Time (minutes)	Synth Beam (mas)	Baseline (m)
99	2017.1.00497.S	2017-10-12	158	45 × 36 at PA 47	40–16200
224	2016.1.00165.S	2017-09-19	44	39 × 19 at PA 66	40–10500
340	2016.1.00165.S	2017-11-08	45	26 × 11 at PA 58	90–12900

using several molecular spectral lines that trace key structures in SrcI to look for signatures of accretion in SrcI.

2. Observations

We used data at 223 GHz (ALMA Band 6; B6) and 340 GHz (ALMA Band 7; B7) as described in A. Ginsburg et al. (2018). These data were processed into images using both uniform and natural weighting of the u–v data. Brigg's visibility weighting was set to robust = 0 to avoid the excessive weight being given to visibilities in relatively sparsely filled regions of the u–v plane by uniform weighting. For naturally weighted images, we set robust = 2 to map the low-brightness, more extended emission. The observational parameters are given in Table 1 for the uniformly weighted u–v data.

Within these bands, several molecular species have been identified as present in SrcI: SiO, SiS, H_2O, NaCl, and SO. Based on the shape and location of the emission from these lines, SiO and SiS have been interpreted as tracers of a wide-angle outflow along the minor axis of a circumbinary disk, while H_2O and NaCl have a strong presence on the surface of/within the circumbinary disk. The structure of SO is more complex and will be further explored in later sections.

The high opacity at 220–330 GHz of the continuum emission from the SrcI disk conceals the internal structure of the disk. The less opaque 99 GHz continuum observations from M. Wright et al. (2022) will also be analyzed as they reveal details of the disk's structure. Emission from molecules associated with the disk gives us information about the structure and kinematics of the SrcI disk and its interaction with the material in its immediate environment.

Hereafter, we discuss the specific molecular lines ^{28}SiO, ^{29}SiO, SiS, H_2O, NaCl, and SO to analyze the structure and kinematics of molecular lines closely associated with SrcI for evidence of accretion. The spectral lines discussed in this paper are listed in Table 2.

Table 2
Spectral Lines

Molecule	Transition	Frequency (GHz)	Upper Energy (K)
^{28}SiO	$v = 0$, $J = 5$–4	217.105	14.5
^{29}SiO	$v = 0$, $J = 5$–4	214.385	30.9
SiS	$v = 0$, $J = 12$–11	217.818	68.0
H_2O	5(5, 0), $v_2 = 1$–6(4, 3), $v_2 = 1$	232.687	3461.9
NaCl	$v = 1$, $J = 18$–17	232.510	625.7
NaCl	$v = 2$, $J = 17$–16	217.980	1128.4
SO	$^3\Sigma v = 0$, $J = 5$–4	215.221	44.1
SO	$^3\Sigma v = 0$, $J = 8$–7	344.311	87.5

3. Results

In this section, we present the spectral line data as the average intensity and average velocity of the emission across the spectral line. These were derived from the intensity and velocity of each spectral channel. The contours map the intensity of the emission. This may be expressed in units of Jy beam^{-1} or Kelvin. We give the equivalent Rayleigh–Jeans brightness in Kelvin for the peak value in the image. The average velocity is shown as a color scale in units of kilometers per second.

3.1. The Molecular Outflow; SiO and SiS

Figure 1 shows the 217.105 GHz ^{28}SiO $v = 0$ ($J = 5$–4) emission with a peak brightness of 1078 K at a velocity resolution of 2 km s^{-1}. This figure also shows 214.385 GHz ^{29}SiO $v = 0$ ($J = 5$–4) emission with a peak brightness of 18,300 K at a velocity resolution of 2 km s^{-1}. The high peak brightness temperature of the ^{29}SiO emission indicates the presence of masers.

Figure 2 shows the 217.818 GHz SiS $v = 0$ ($J = 12$–11) emission with a peak brightness of 409 K with a velocity resolution of 2 km s^{-1}. The SiS emission traces a shell-like structure along the boundaries of the SiO outflow (M. Wright et al. 2020). This higher-resolution SiS image reveals the complex structure it traces.

3.2. SO

Figure 3 shows the 344.31 GHz SO emission with natural weighting of the $u-v$ data to emphasize the larger scale structure. The peak brightness with 1 km s^{-1} velocity resolution is 375 K.

3.3. H_2O and NaCl Emissions

Figure 4 shows the H_2O and NaCl emissions. The 232.687 GHz H_2O line (5(5,0), $v_2 = 1$–6(4,3), $v_2 = 1$) is more closely associated with the SrcI disk than the SiO and SiS, which primarily trace the molecular outflow.

Figure 4 also shows the 232.51 GHz NaCl $v = 1$ ($J = 18$–17) emission with a peak brightness of 197 K with a velocity resolution of 2 km s^{-1}.

4. Discussion

In this section, we discuss each of the molecular lines observed and the regions of the disk and outflow that each traces. The distribution of the molecular lines depends on the formation and destruction of the molecules, and we include a discussion of the chemical interactions between the outflow and ambient material. The structure and kinematics of the SiS suggest that ambient material may be entrained into the molecular outflow leading to the export of angular momentum from the outflow. We discuss the evidence for Bondi–Hoyle–Lyttleton (BHL) accretion onto the disk around Source I, and the evolution of the disk and the protostar(s).

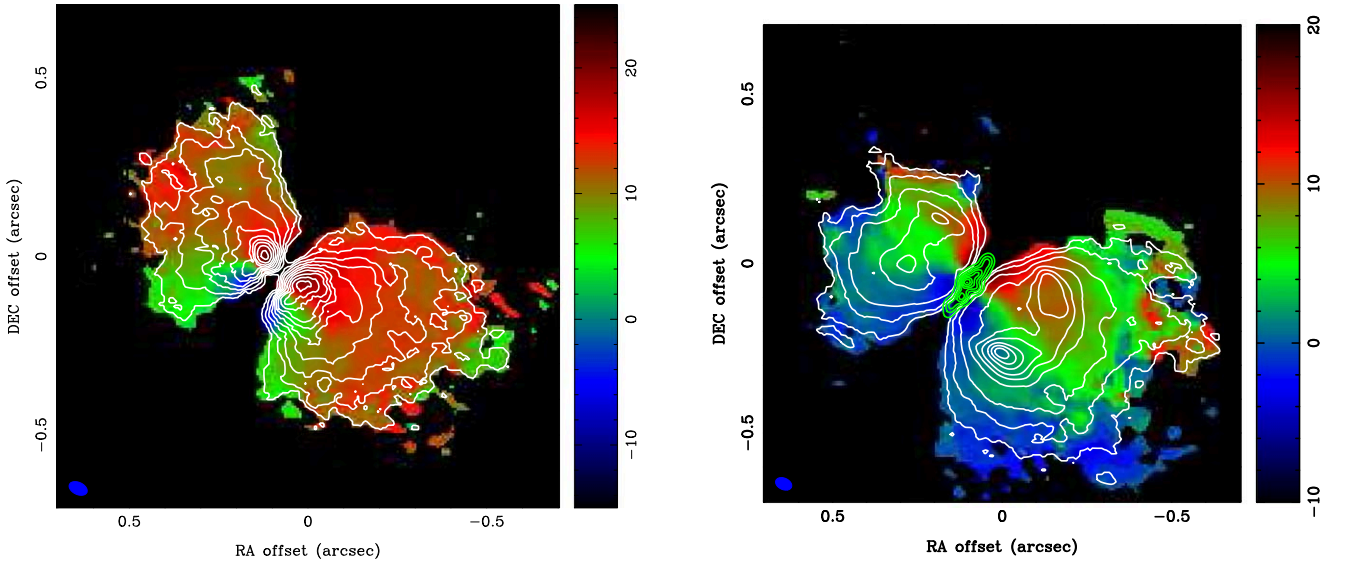

Figure 1. SiO and ^{29}SiO emission from −20 to +30 km s^{-1}. (Left) The color image shows the moment 1 velocity image for the 217.10 GHz SiO $v = 0$ $J = 5$–4 with velocities from −15 to +25 km s^{-1} indicated in the color wedge. The peak brightness with 2 km s^{-1} velocity resolution is 1078 K. The white contours show the SiO emission, integrated over −20 to +30 km s^{-1}, at 1, 3, 5, 7, 9, 11, 13, 15, 17, 19 mJy beam^{-1}. (Right) The color image shows the moment 1 velocity image for the 214.39 GHz ^{29}SiO $v = 0$ $J = 5$–4 emission with velocities from −10 to +20 km s^{-1} indicated in the color wedge. The peak brightness with 2 km s^{-1} velocity resolution is 18,300 K, indicating maser emission. The white contours show the ^{29}SiO emission, integrated over −20 to +30 km s^{-1}, at 2.5, 5, 10, 20, 30, 40, 60, 80, 100 mJy beam^{-1}. The green contours near the center show the 99 GHz continuum emission with contours at 1, 2, 3, 4, 5, 6, 7, 8 mJy beam^{-1}. Both SiO isotopes trace the wide-angle outflow along the minor axis of the disk, with a clear velocity gradient along the major axis close to the disk. Further from the disk, the velocity pattern has a more complex structure. The synthesized beam for the SiO emission (FWHM 54 × 34 mas, PA 65°) is indicated in blue in the lower left. The continuum data have been convolved by a 30 mas FWHM beam.

4.1. The Bipolar Outflow

T. Hirota et al. (2017) fitted a hollow cone model to the 484.056 GHz Si^{18}O $J = 12$–11 line and constrained the launching radius and outward velocity of the outflow to be >10 au and ∼10 km s^{-1}, respectively. From these results, T. Hirota et al. (2017) concluded that the rotating outflow in SrcI is likely driven by a magneto-centrifugal disk wind. T. Hirota et al. (2017) note that the critical density required to excite the $J = 12$–11 transition (6×10^7 cm^{-3}) is higher than those of $J = 2$–1 at 86 GHz (3×10^5 cm^{-3}) and $J = 5$–4 at 217 GHz (4×10^6 cm^{-3}). Additionally, the ^{28}SiO molecular line may be highly opaque, as discussed by J. A. López-Vázquez et al. (2020). The Si^{18}O isotopologue is expected to be optically thin, as it traces regions of higher density than the optically thick Si^{16}O lines.

Both SiO isotopes shown here in Figure 1 clearly trace the wide-angle outflow in SrcI, with the velocity structure growing in complexity away from the disk. In Figure 1, a clear velocity gradient across the (projected) minor axis of the disk can be seen in regions close to the central source. The smooth blue–green–red transition from SE–NW indicates that the rotational velocity of these molecules dominates in these regions. Further away from the center, the smooth velocity gradient disappears and the velocities become "mixed." The ^{28}SiO image shows little blueshifted emission beyond the small amount present close to the center, with the outer regions of the outflow dominated by an irregular patchwork of green and redshifted emission. A similar pattern can be seen in the ^{29}SiO. These features are roughly consistent with the rotating expanding model presented by T. Hirota et al. (2017). Figure 5 shows the velocity channel maps of the outflow seen in SiO and SiS emission. At 54 × 34 mas (22 × 14 au) resolution, the SiS image shows a shell-like structure. The visible velocity structure suggests that there is a turbulent layer on the outside of the SiO emission.

Figure 6 shows the 214.39 GHz ^{29}SiO $v = 0$ $J = 5$–4, and 217.82 GHz SiS $v = 0$ $J = 12$–11 emission integrated over −10 to +20 km s^{-1}. Four cuts are drawn across the outflow: along the outflow edges (PA = 122° and 172°), along the circumbinary disk major axis (PA = 142°), and along the outflow axis (PA = 52°).

Figure 7 shows position–velocity profiles for ^{29}SiO emission along these four cuts. Two of these cuts (PA = 122° and 172°) are along the edges of the outflow. The line-of-sight velocity widths decrease from the full width of the ^{29}SiO emission close the the disk (−20 to +30 km s^{-1} at 0″) to ∼−5 to +15 km s^{-1} at ∼0.″2 to 0.″3 (80–120 au) from the disk.

The position–velocity profile along the disk's major axis (PA = 142°) follows the rotation of the disk with strong absorption at redshifted velocities. The position–velocity profile along the disk minor axis (PA = 52°) measures the radial expansion velocity, with small contributions, $v_z \times \cos(i)$, from the outflow velocity along the minor axis, and from the rotation velocity. The line-of-sight velocity along the disk's minor axis is ∼−5, and ∼+15 km s^{-1} from the front and back side of the outflow.

4.2. Entrainment of Ambient Material into the Molecular Outflow?

Figure 8 shows position–velocity profiles for SiS emission along these four cuts. The SiS emission shows a more complex structure than SiO. Along the edges of the outflow (PA = 122° and 172°), the line-of-sight velocity range is consistently centered around the systemic velocity of SrcI (∼+5 km s^{-1}). The velocity width decreases from its maximum (∼−14 to +24 km s^{-1}) close the the disk to ∼−5, and +15 km s^{-1} at ∼0.″4 (160 au) from the disk. The line-of-sight velocity along

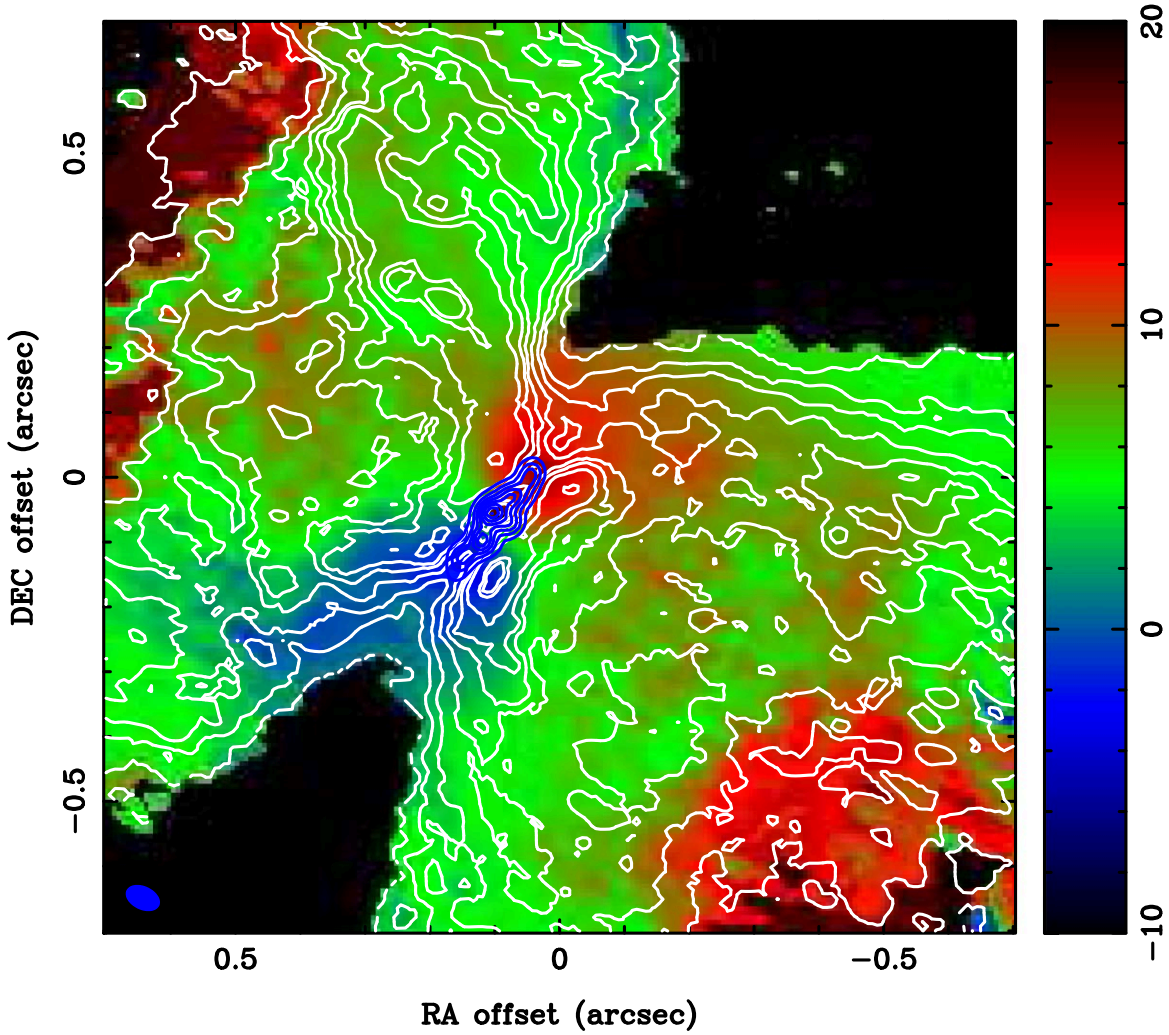

Figure 2. SiS emission from −10 to +20 km s^{-1}. The color image shows the moment 1 velocity image for the 217.82 GHz SiS $v = 0$ $J = 12$–11 emission with velocities from −10 to +20 km s^{-1} indicated in the color wedge. The peak brightness with 2 km s^{-1} velocity resolution is 409 K. The white contours show the SiS emission, integrated over −20 to +30 km s^{-1}, with contours at 20, 60, 90, 130, 170, 200, 240, 320, 340 mJy beam^{-1} × km s^{-1}. The blue contours show the 99 GHz continuum emission with contours at 1, 2, 3, 4, 5, 6, 7, 8 mJy beam^{-1}. There is a clear velocity gradient along the major axis close to the disk. Further from the disk, SiS has a more complex spatial and velocity structure. The synthesized beam for the SiS emission, (FWHM 54 × 34 mas, PA 66°), is indicated in blue in the lower left. The continuum data have been convolved by a 30 mas FWHM beam.

the edges of the outflow measures the rotation velocity, $v_\phi \times \sin(i)$, where i is the inclination of the disk to the line of sight. Assuming a disk inclination of 80° to 85°, there are small contributions from the radial expansion velocity, $v_r \times \cos(i)$, and the outflow velocity along the minor axis, $v_z \times \cos(i)$. Both ^{29}SiO and SiS show that the rotational velocity decreases with distance from the disk, consistent with the results shown by T. Hirota et al. (2017) for the Si^{18}O $J = 12$–11 line.

Multiple velocity components can be seen along the edges of the outflow in Figures 7 and 8.

The position–velocity profile along the disk major axis (PA = 142°) follows the rotation of the disk. The SiS is not seen in absorption along the major axis of the disk.

The position–velocity profile along the disk minor axis (PA = 52°, lower-right subimage of Figure 8) measures the radial expansion velocity, with smaller contributions from the outflow velocity along the minor axis, and the rotation velocity. The line-of-sight velocity in SiS along the disk minor axis increases in a parabolic fashion, i.e., more rapidly close to the disk. Gaussian fits to the spectra along the minor axis show that the line-of-sight velocity of the SiS emission is initially centered at the system velocity at regions close to the disk (∼+5 km s^{-1} at <0.″1 (40 au) from the disk). This diverges into two distinct, much thinner velocity structures in either direction away from the disk. The NE outflow has velocity structures centered at ∼−8 and ∼+17 km s^{-1} (at ∼+0.″3). The SW outflow has structures centered at ∼−4 and ∼+17 km s^{-1} (at ∼−0.″3). As expected, this two-pronged velocity structure is due to the contributions of the far and close sides of the outflow.

The radial velocity is ∼4 km s^{-1} more blueshifted on the NE side of the disk. Assuming the same opening angle of the outflow on both sides of the disk, this difference in the line-of-sight velocity along the disk minor axis measures the outflow velocity, $v_z \times \cos(i)$, where i is the inclination of the disk to the line of sight. Assuming a disk inclination of 80°–85°, the implied outflow velocity is $v_z \sim 23$ to 45 km s^{-1}.

For comparison, T. Hirota et al. (2017) found, using the 484 GHz Si^{18}O line, a radial velocity (v_r) between ∼8 and 12 km s^{-1} and a rotation velocity (v_ϕ) that decreases from ∼7 km s^{-1} at 50 au from the disk to ∼2 km s^{-1} at 150 au from the disk.

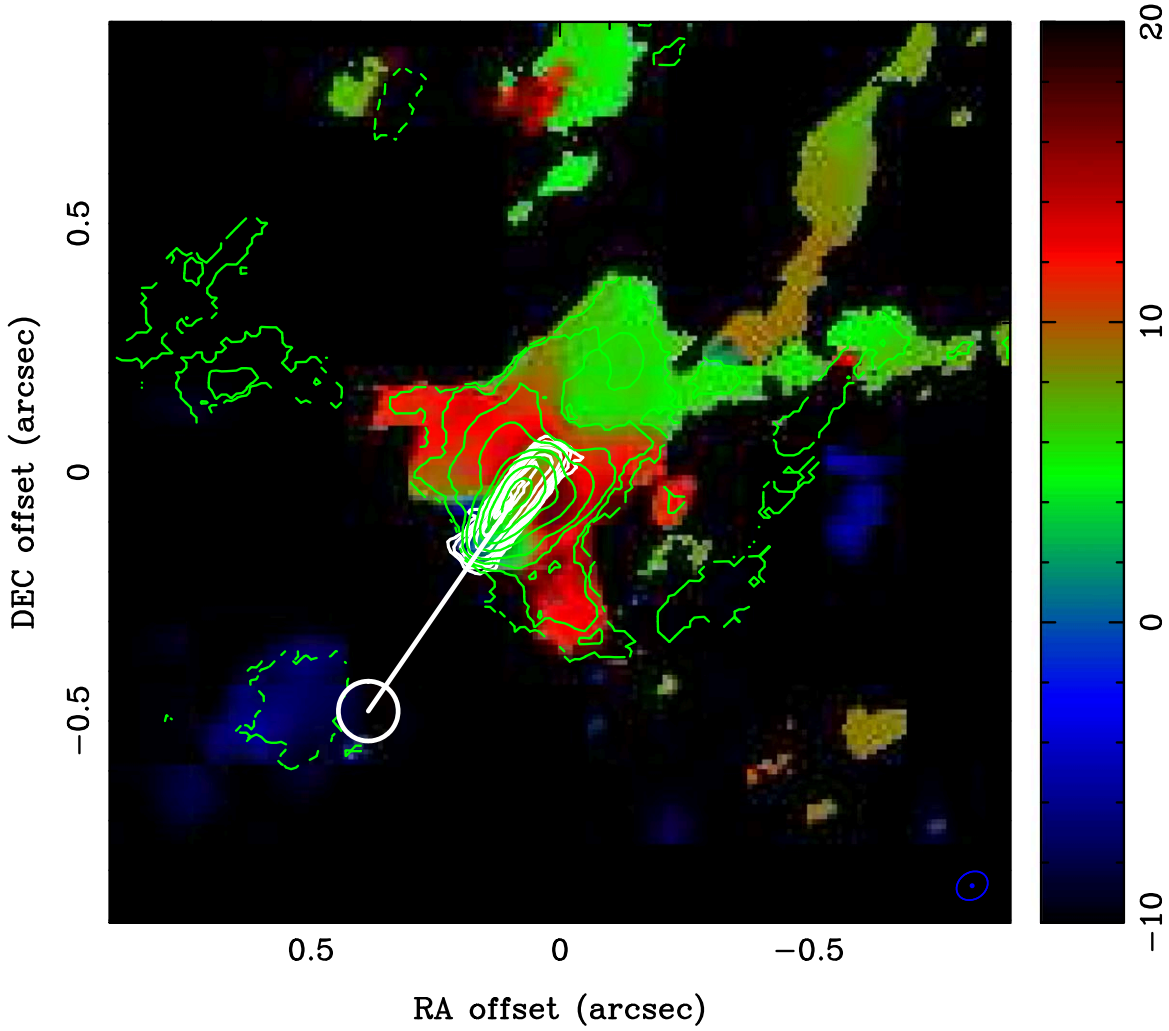

Figure 3. SO 344.31 GHz emission with natural weighting of the $u-v$ data to emphasize the larger scale structure. The color image shows the moment 1 velocity image with velocities from −10 to +20 km s^{-1} indicated in the color wedge. The peak brightness with 1 km s^{-1} velocity resolution is 375 K. Green contours show the SO emission integrated over a velocity range of −20 to +30 km s^{-1}. Contour levels are at −0.5, −0.2, 0.1, 0.2, 0.5, 1.0, 2.0, 3.0, 4.0, 5.0 Jy beam^{-1} × km s^{-1}. The SO line shows an envelope of emission around the disk, with a steep gradient at the SE end of the disk, and an extended tail to the NW of the disk. There are also emission features to the NE and SW which trace the outflow from the disk as seen in SiO and SiS emission. The synthesized beam FWHM (66 × 54 mas, PA −56°) is indicated in blue in the lower right. White contours show the 340 GHz continuum emission from the disk at 10 mas resolution. Contour levels are at 25, 50, 100, 200, 400, 500, 600, 700, 800 K. The white vector shows the proper motion of SrcI in 100 yr. The open circle radius shows the rms error in 100 yr (L. F. Rodríguez et al. 2017).

The relative velocity of the ambient material is roughly parallel to the plane of the disk and perpendicular to the direction of the outflow. In consequence, the wide-angled nature of the outflow poses a significant disruption to the flow of the ambient material around SrcI.

Additionally, the outflow appears to be comoving with the disk. It is not swept back by ram pressure from its motion through the medium. Material ejected from the disk earlier in its trajectory seems to move in tandem with the disk. Naturally, this raises the question of how this ejected material maintains its momentum and connection to the central disk.

A possible explanation is that the outflow is being stiffened by magnetic fields (T. Hirota et al. 2020). It is also possible that the outflow's density when compared to the external medium, is high enough to render the effect of motion negligible. The outflow from SrcI has a larger cross section than the edge-on disk and intercepts the ambient medium which it is moving through. Assuming an ambient density, $n[H_2] \sim 1.6 \times 10^5$ cm^{-3} (R. L. Snell et al. 1984), a velocity of 10 km s^{-1}, and cross-sectional dimensions of 1000 × 200 au for the SrcI outflow, the ambient mass flow is $\sim 10^{-5}\,M_\odot$ yr^{-1}, or $\sim 5 \times 10^{-3}\,M_\odot$ over the ∼550 yr since the BN/SrcI encounter. This is comparable to the estimated mass in the outflow, which ranges from 10^{-5} to $10^{-3}\,M_\odot$ yr^{-1}. These estimates may be affected by the motion of SrcI through the BN/SrcI explosion debris (M. Wright et al. 2022).

It is notable that J. A. López-Vázquez et al. (2020) fitted position–velocity profiles to SiO and SiS lines and found that a model of a rotating molecular envelope accreting onto the outflow (R. K. Ulrich 1976) was not a good fit to the data. However, the dilution of the rotational velocity with the distance from the disk (as noted above) suggests that some of the ambient material may be entrained by the rotating outflow. In laboratory experiments, C. Pillich et al. (2021) found that dry silicate dust becomes more sticky as the temperature increases, by a factor of ∼10 up to 1000 K, and then by another factor of ∼100 for temperatures of ∼1200 K. Compression and shock heating of the envelope of the outflow may thus make

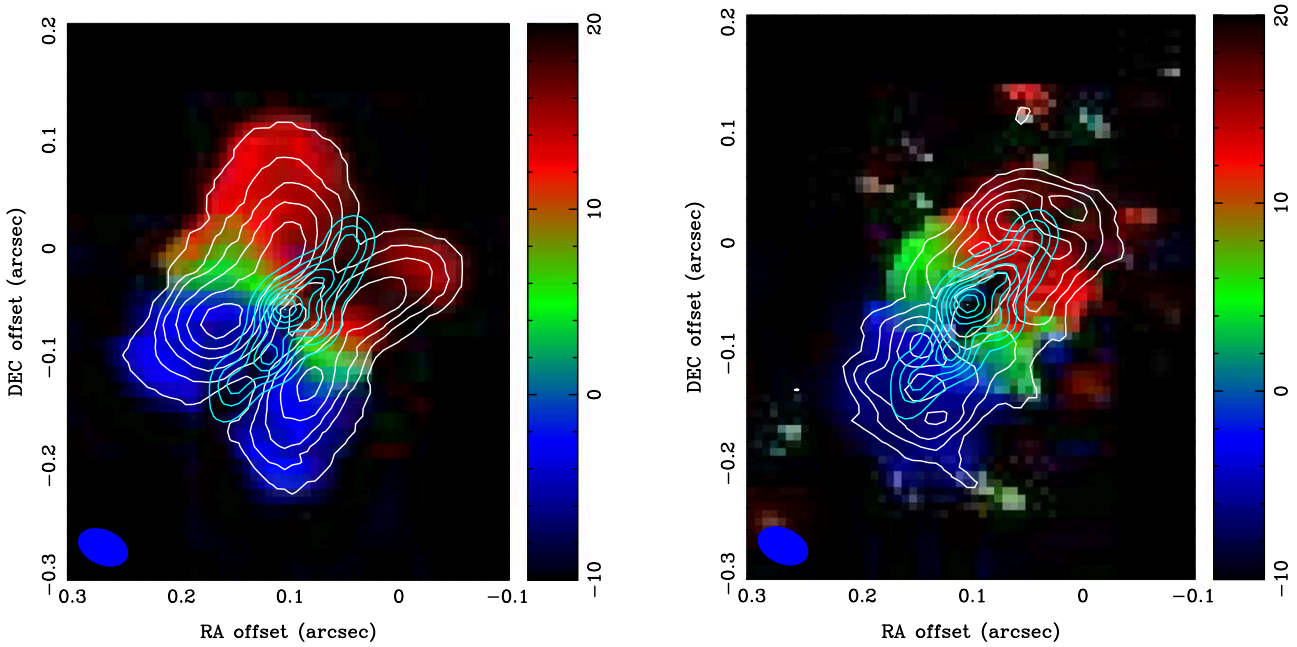

Figure 4. H_2O and NaCl emission from −10 to +20 km s^{-1}. (Left) The color image shows the moment 1 velocity image for the 232.69 GHz H_2O emission with velocities from −10 to +20 km s^{-1} indicated in the color wedge. The peak brightness with 2 km s^{-1} velocity resolution is 1200 K. The white contours map the moment 0 velocity image of the H_2O emission integrated over −20 to +30 km s^{-1} at contour levels of 1, 4, 7, 11, 15, and 19 mJy beam^{-1}. (Right) The color image shows the moment 1 velocity image for 232.51 GHz NaCl $v = 1$ $J = 18$–17 emission with velocities from −10 to +20 km s^{-1} indicated in the color wedge. The peak brightness with 2 km s^{-1} velocity resolution is 196 K. The white contours show the NaCl emission, integrated over −20 to +30 km s^{-1}, at 1, 4, 7, 11, 15, 19 mJy beam^{-1}. The blue contours show the 99 GHz continuum emission with contours at 1, 2, 3, 4, 5, 6, 7, 8 mJy beam^{-1}. Both NaCl and H_2O show a strong velocity gradient along the disk's major axis. The NaCl emission is more closely associated with the continuum disk and extends to greater radii along the disk major axis than the H_2O emission. The synthesized beam for the NaCl, and H_2O (FWHM 47 × 31 mas, PA 66°) is indicated in blue in the lower left. The continuum data have been convolved by a 30 mas FWHM beam.

adhesion and entrainment of some ambient material into the outflow more likely.

A final point of note is that the SiS emission does not extend all the way to the disk surface, unlike the SiO (refer to Figure 2). The parabolic increase in the radial velocity (v_r) at ∼40–80 au from the disk where the brightest SiS emission is located could result from ambient material being funneled between the disk and the outflow (refer to Figure 8). The velocity difference between the ambient material and the rotating outflow would result in shocks and heating of the outflow. Note that it is at this distance from the disk where the outflow expands and changes from corotation with the disk, and ground state SiO masers appear in the $J = 1$–0 and $J = 2$–1 transitions (L. J. Greenhill et al. 2013; T. Hirota et al. 2020).

L. J. Greenhill et al. (2013) suggested that shocks resulting from a decrease in the Alfvén velocity to a point below the outflow velocity may trigger the appearance of maser emission in the outflow at ∼100 au. Shock heating from the flow of ambient material funneled between the disk and the outflow provides an alternative explanation consistent with our SiS observations. The SiS maps the boundary of the outflow mapped in SiO, suggesting chemical interactions between the outflow and ambient material.

4.3. Chemical Interactions between the Outflow and Ambient Material

J. Li et al. (2015) studied the sulfur chemistry in 36 sources in massive star-forming regions, observing OCS, $O^{13}CS$, ^{13}CS, H_2S, and SO transitions. Their results suggest that H_2S is likely the primary sulfur-carrying molecule in massive hot cores. The column density and abundance of OCS were generally higher than CS and SO as well. The hot core model of Orion-KL could reproduce the general trend (H_2S > OCS > CS > SO) observed in this paper. H_2S is likely to be the most abundant gas-phase sulfur-containing molecule in hot massive cores. Since hydrogenation is expected to be the most efficient process on grains, H_2S could be formed on interstellar grains (E. F. van Dishoeck & G. A. Blake 1998). During the cold collapse phase of star formation, sulfur atoms freeze out onto grains and remain there in the form of H_2S until core heating begins. At this point, H_2S is evaporated from the grains and rapidly undergoes reactions that drive the production of SO and SO_2 (S. B. Charnley 1997; V. Wakelam et al. 2005, 2011). The initial destruction of H_2S by H_3O^+ is more efficient in high-mass protostars compared to lower-mass ones as water is more abundant (F. F. S. van der Tak et al. 2006).

The observed SiS shell around the outflow may be produced in shocks from S-bearing molecular species in the ambient medium and SiO (or other Si-bearing molecules) in the outflow. Models by G. Pineau des Forets et al. (1993) of C-type shocks with velocities between 5 and 40 km s^{-1} and densities between 10^4 and 10^6 cm^{-3} showed an enhancement of SO and SO_2 abundances by 2 orders of magnitude. SO decreases quickly after the passage of a shock, while SO_2 is enhanced during and for some time after the shock. The relative velocity of the ambient medium from the proper motion of SrcI and the rotation and expansion velocity of the disk and outflow provide a range of shock velocities between ∼0 and 30 km s^{-1}.

Figure 6 shows that the SiS has a complex structure, which may be evidence for this turbulent mixing. However, reactions with both atomic hydrogen and atomic oxygen will both destroy SiS rapidly. We can estimate a timescale from the SiS

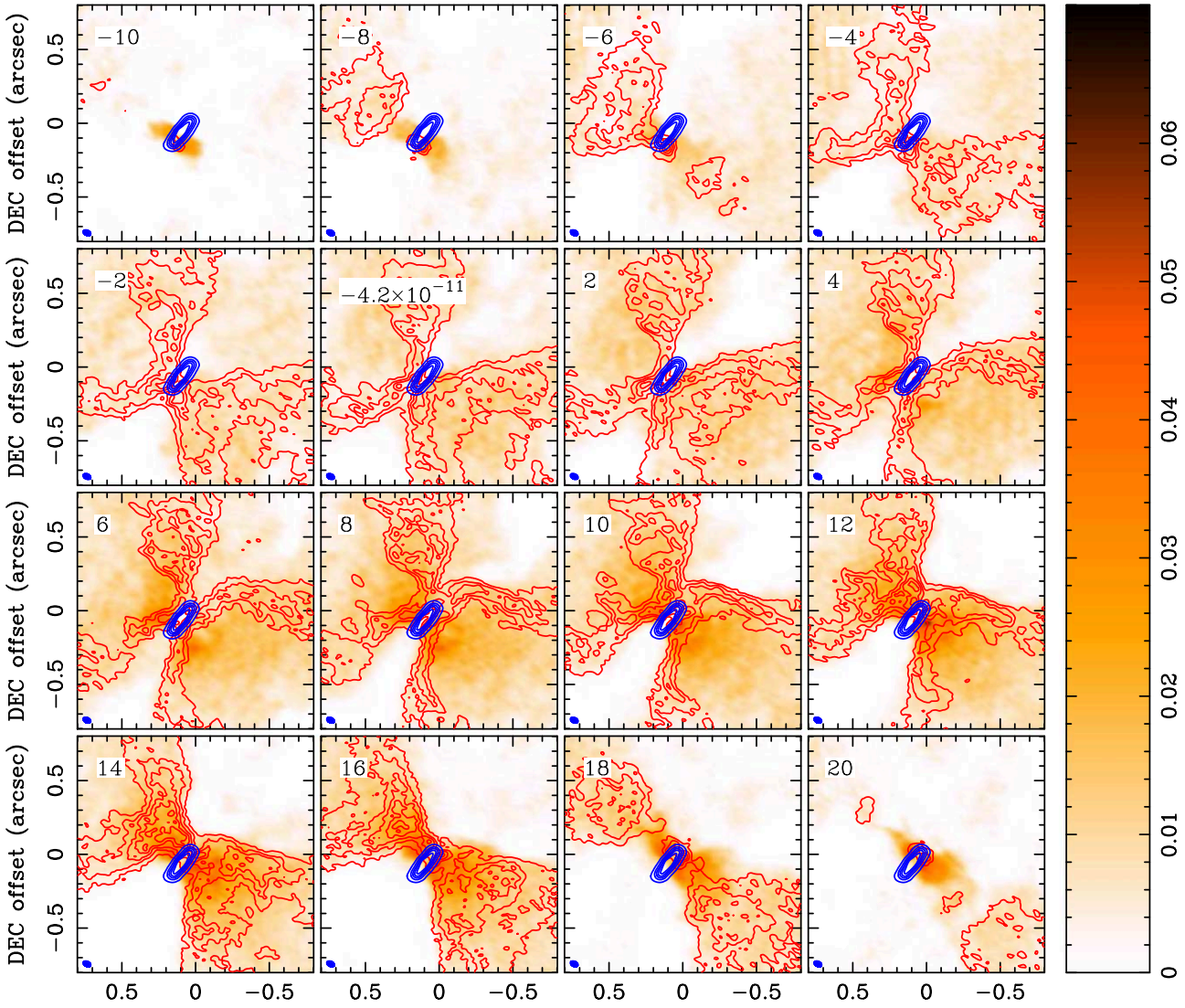

Figure 5. Outflow from the SrcI disk mapped in SiO and SiS emission. The color image shows SiO (217.10498 GHz) in 2 km s^{-1} channels with brightness from 0 to 0.07 Jy beam^{-1} indicated in the color wedge. LSR velocities in km s^{-1} are shown in the upper left. Red contours show SiS 217.81766 GHz emission in 2 km s^{-1} channels, with contour levels of 5 10 15 20 25 mJy beam^{-1}. Blue contours show a 218 GHz continuum with contour levels of 5 10 15 20 25 mJy beam^{-1}. The SiS emission traces a shell-like structure along the boundaries of the SiO outflow. The synthesized beam FWHM 54 × 34 in PA 65° is indicated in blue in the lower left.

layer thickness and the diffusion/turbulent velocity. Estimating a thickness of 40 au and velocity of ∼10 km s^{-1} from the observed SiS images, we would expect the SiS to persist for ∼20 yr after formation.

Finally, we make note of a possible chemical interaction occurring between the SiO in the outflow and the SO in the ambient medium. M. Wright et al. (2020) found that SiS appears to map the boundary layer of the SiO outflow, and corotates with the SiO. This raises questions about the potential role of SO in the formation chemistry of SiS.

Several studies have examined potential formation pathways for SiS in recent years, motivated by its proposed key role in the formation of sulfide dust grains (S. Doddipatla et al. 2021). Three pathways to forming SiS are worth consideration:

$$\mathrm{Si + SH \longrightarrow SiS + H} \quad (1)$$

$$\mathrm{Si + H_2S \longrightarrow SiS + H_2} \quad (2)$$

$$\mathrm{SiH + S \longrightarrow SiS + H.} \quad (3)$$

M. A. M. Paiva et al. (2020) have shown that Reaction (1) is exothermic and barrierless. Reaction (2) is exothermic (M. A. M. Paiva et al. 2020), and computational work by S. Doddipatla et al. (2021) suggests that substantial SiS can be formed by this pathway as H_2S is abundant in this region. Reaction (3) is also exothermic and barrierless but can produce Si + SH instead, and the branching ratios are not yet known (M. Rosi et al. 2018). The remaining question is then the source of the reactants.

In SrcI, with the SiS emission tracing the outer edges of the outflow, Si could be readily produced in shocks. Since the SiO outflow corotates with the disk close to the disk and then mushrooms out with a blended rotation signature, shocks may occur as the outflow imparts angular momentum to ambient material, which creates and can be mapped in SiS. Both SH and H_2S are similarly known to be enhanced in shocked regions, being liberated from ice mantles (D. A. Neufeld et al. 2012). H_2S abundances are enhanced by a factor of 1000 in the Orion hot core and the "plateau" $[H_2S/H_2] \sim 10^{-6}$ relative to quiescent clouds (Y. C. Minh et al. 1990). The large abundance of H_2S in the hot core may result from grain mantle evaporation, while the large abundance in the plateau could

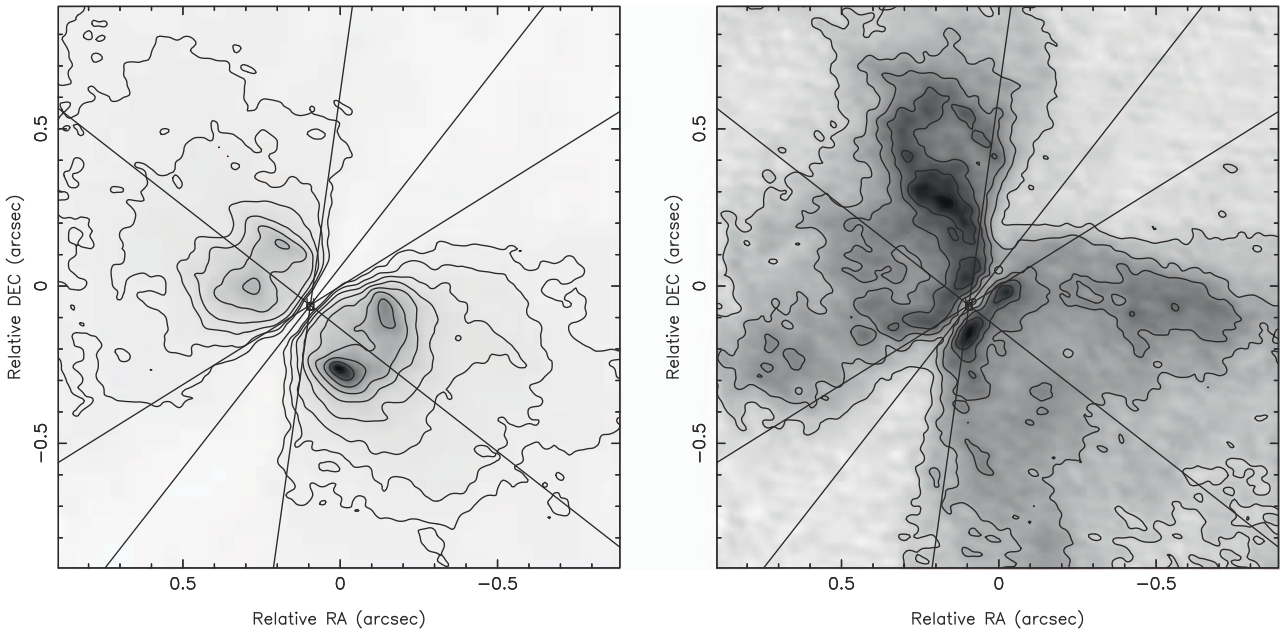

Figure 6. ^{29}SiO and SiS emission integrated over −10 to +20 km s^{-1}. The four lines are drawn along the outflow edges in position angles 122° and 172°, along the circumbinary disk major axis in position angle 142°, and along the outflow axis in position angle 52°. Left: ^{29}SiO 214.39 GHz. Right: SiS 217.82 GHz.

result from high-temperature gas-phase chemistry and/or grain-surface chemistry (Y. C. Minh et al. 1990).

The plateau emission comes from the outflow associated with SrcI where shock chemistry may also be responsible for the large abundances of SO, SO_2, H_2S, and SiO. H_2S and $H_2^{34}S$ with $E_u < 500$ K are seen as blueshifted absorption features at 0.″2 resolution indicating that they originate in outflowing gas (R. L. Plambeck & M. C. H. Wright 2016). Detailed shock models (M. L. van Gelder et al. 2021) found that SO and SO_2 are good tracers of accretion shocks. Desorption of SO and SO_2 ices can occur in high-velocity (>5 km s^{-1}) shocks at high densities (>10^7 cm^{-3}). They found that the abundances of atomic S and O, and in ices such as H_2S, CH_4, SO, and SO_2 play a key role in the abundances of SO and SO_2 that are reached in the shock. Reaction (3), on the other hand, is harder to justify as important in our case. While M. Rosi et al. (2018) show that this reaction is exothermic and barrierless, the source of sufficient SiH to produce our observed quantities of SiS is unclear. To date, SiH has only been tentatively identified in space (albeit in Orion-KL) using Caltech Submillimeter Observations (P. Schilke et al. 2001).

Our observed coincidence of SiS with SO suggests another pathway might be viable,

$$\mathrm{SO} + \mathrm{SiO} \longrightarrow \mathrm{SiS} + \mathrm{O_2}. \quad (4)$$

D. R. Campanha et al. (2022) studied the reverse reaction,

$$\mathrm{SiS} + \mathrm{O_2} \longrightarrow \mathrm{SiO} + \mathrm{SO}, \quad (5)$$

which they showed possesses a substantial activation barrier. While this might suggest that the forward reaction is efficient, in fact, their potential energy surface (their Figure 3) indicates that both forward and reverse reactions possess entrance barriers and that the forward reaction to form SiS is substantially endothermic, but could be driven by shock heating. These endothermic reactions may prove to be important in the brief, high-temperature regime of interstellar shocks (A. M. Burkhardt et al. 2019). Extensive modeling work would be needed to determine the extent of the effect on the overall chemistry. Further computational or experimental work exploring other potential pathways between these species is warranted.

One potential reaction that has not been, to our knowledge, well studied is that between SiH and SH:

$$\mathrm{SiH} + \mathrm{SH} \longrightarrow \mathrm{SiS} + \mathrm{H_2}. \quad (6)$$

There also remain some open questions about the relationship between SiS and H_2O, which may be especially relevant given the excited H_2O present at the base of the outflow in SrcI. Taken as a whole, and given the spatial overlap of many of these molecules in SrcI, further observations at high resolution in SrcI particularly targeting SiS, SiO, SiH, SH, H_2S, SO, SO_2, and H_2O are warranted.

4.4. H_2O in the Outflow

The origin of this water line in the gas phase is not clear. The H_2O emission extends deeper and likely formed in the disk, but icy grain mantles are unlikely to have survived in the hot disk for ∼550 yr since the BN/SrcI encounter. Hydrated minerals are another possible source of H_2O. The AlO line emission that was mapped in the outflow close to the disk suggests that refractory grain cores and grain mantles are destroyed (M. Wright et al. 2020). Carbon grains are destroyed at ∼800–1150 K, silicate grains are evaporated at ∼1300 K, and AlO at ∼1700 K (P. Lenzuni et al. 1995).

This vibrationally excited water line is also detected in the Keplerian disk around the O-type protostar G17.64+0.16 (L. T. Maud et al. 2019) and in the O-type protobinary system IRAS 16547-4247 (K. E. I. Tanaka et al. 2020). The H_2O $v_2 = 1$ emission with $E_u = 3464$ K is concentrated at the positions of protostars (K. E. I. Tanaka et al. 2020) and in several other high-mass protostellar objects (A. Ginsburg et al. 2023).

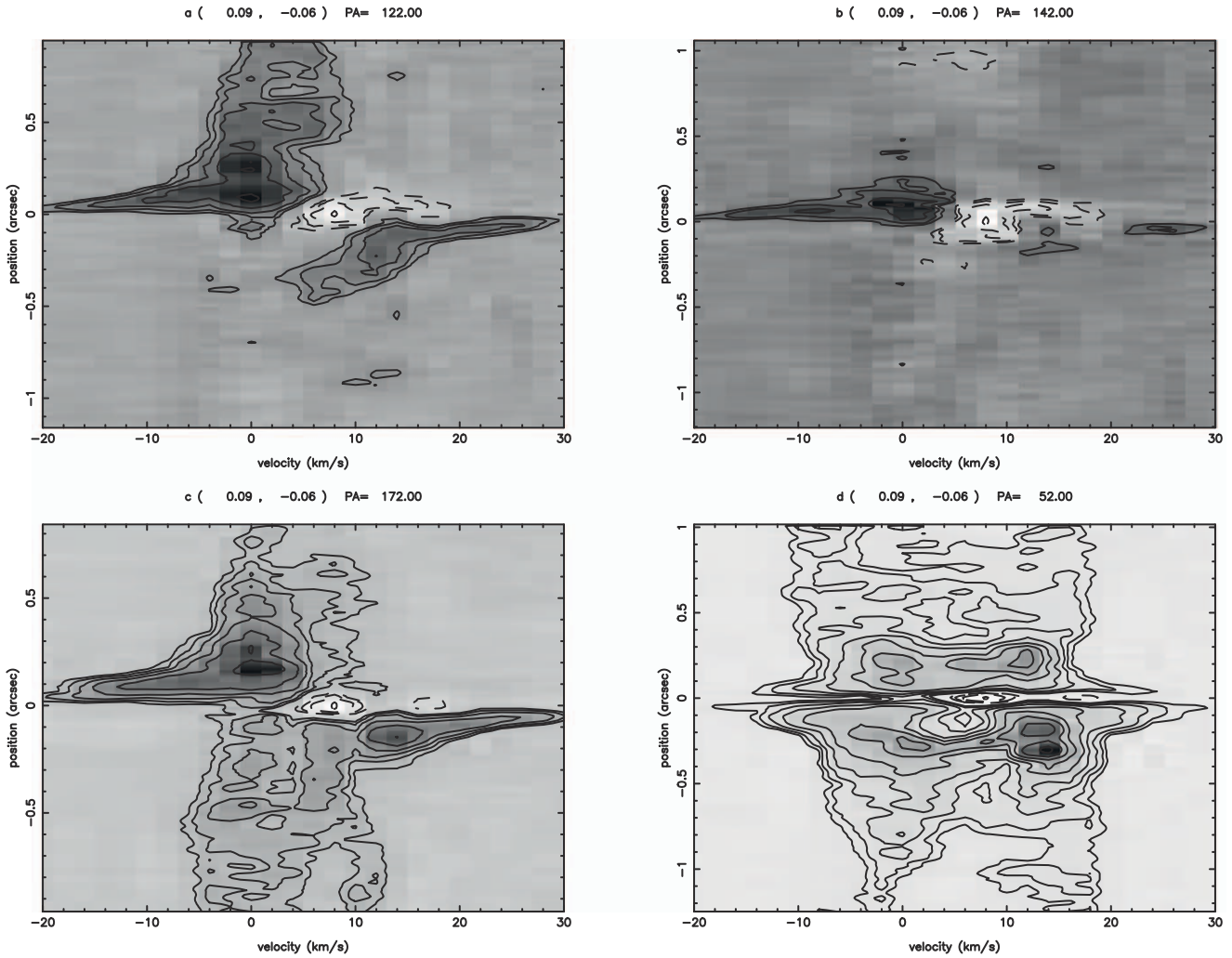

Figure 7. Position–velocity contours for ^{29}SiO emission. Position–velocity contours for the 214.39 GHz ^{29}SiO $v = 0$ $J = 5$–4 emission along the outflow edges in position angles 122° and 172°, along the circumbinary disk major axis in position angle 142°, and along the outflow axis in position angle 52°. Multiple velocity components are seen along the outflow edges, e.g., the emission at 10–12 km s^{-1} in PA 172° in panel (c).

Near IR observations of H_2O toward the massive protostar AFGL 2136 IRS 1 identified 47 rovibrational transitions in warm (500 K), dense ($n(H_2) > 5 \times 10^9$ cm^{-3}) gas, suggesting an origin close to the central protostar (N. Indriolo et al. 2013).

On the other hand, Figure 9 shows that H_2O emission peaks are associated with SiS close to the disk, suggesting that heating by shocks may play a role in the formation and dissociation of H_2O, ∼50 au from the SrcI disk, where the rotating SiO column expands abruptly into a turbulent wide-angle outflow. These distributions fit into a scenario where the SiO is formed from grain destruction following the dissociation of H_2O (P. Schilke et al. 1997). In these models, grain mantles and grain cores are destroyed in shocks; Si is released into the gas phase and then oxidized by dissociation products of H_2O.

A. Ginsburg et al. (2018) fitted a Keplerian rotation curve to the envelope of a position–velocity along the major axis of the SrcI disk. However, the butterfly-like shape seen in Figure 4 suggests that the H_2O also has an outflow component.

Figure 9 compares the H_2O emission with the SiS and SiO at ∼50 × 30 mas resolution. At velocities of −18 to −10 and 22 to 30 km s^{-1}, the H_2O traces the SiO outflow along the minor axis of the disk, while at velocities of −8 to 20 km s^{-1}, the H_2O traces the bright SiS emission in the inner part of the SiS outflow.

4.5. Possibility of Bondi–Hoyle–Lyttleton Accretion onto the Circumbinary Disk of Source I

As summarized by R. Edgar (2004), the BHL accretion model describes a possible process of accretion onto a moving point mass passing through a uniform gas cloud. In essence, the gravity of the mass lenses the medium into a trail in its wake. From this dense, aligned column, the mass can accrete. This model neglects pressure and thermal effects, such as the trapping of thermal energy in the trailing column. Accretion onto the disk from the ambient cloud would be limited to roughly the BHL rate, which for $n_{H_2} = 1.6 \times 10^5$ cm^{-3}, $\rho \sim 5 \times 10^{-19}$ g cm^{-3}, $M = 15\,M_\odot$, and $v = 10$ km s^{-1}. relative to the interstellar background is given by

$$\dot{M} = \lambda_* 4\pi\rho \frac{(GM)^2}{(v^2 + c_s^2)^{3/2}} \approx 5 \times 10^{-7} M_\odot \text{ yr}^{-1}, \quad (7)$$

where $c_s = \sqrt{k_B T/\mu m_p}$ is the ambient thermal (sound) speed ∼1–5 km s^{-1} for $T = 10$–1000 K, and $\mu = 2.8$. λ_* is a dimensionless constant of order unity (F. Shu 1991).

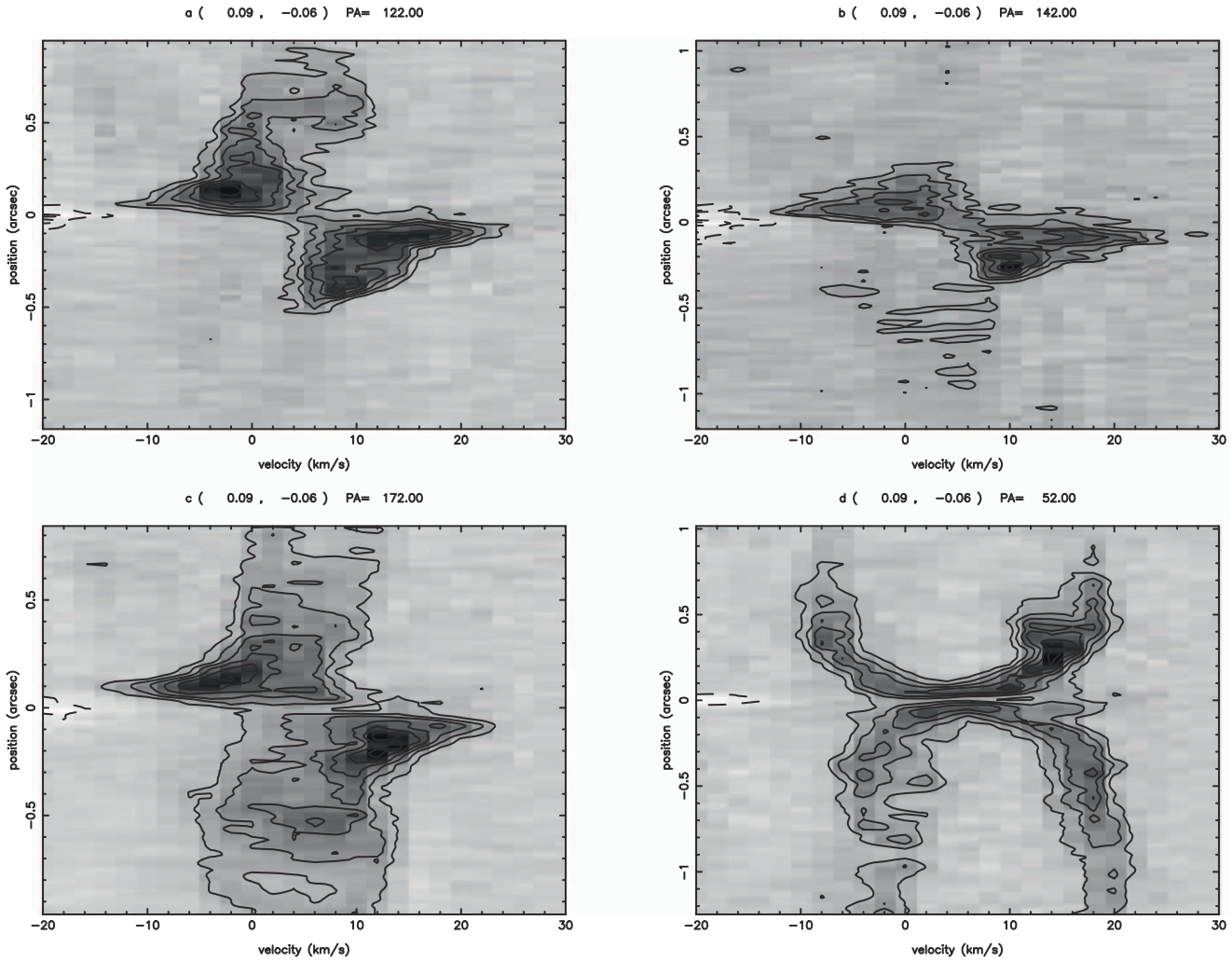

Figure 8. Position–velocity contours for SiS emission. Position–velocity contours for the 217.82 GHz SiS $v = 0$ $J = 12-11$ emission along the outflow edges in position angles 122° and 172°, along the circumbinary disk major axis in position angle 142°, and along the outflow axis in position angle 52°. Multiple velocity components are seen along the outflow edges, e.g., the emission at 10 km s^{-1} in PA 122° in panel (a).

The SO line is a possible tracer of this trailing shocked ambient medium around SrcI resulting from the BN/SrcI explosion. J. Bally et al. (2017) observed the 219.95 GHz SO line with ALMA at 1″ resolution. Figure 17 from M. Wright et al. (2020) shows a 30″ region image centered on SrcI. The SO is seen throughout this region with a similar filamentary structure in the SiO and CO emissions.

Figure 3 shows SO emission around SrcI, and the expected proper motion of SrcI in 100 yr. Table 1 from L. F. Rodríguez et al. (2017) gives the positions and proper motions of the runaway stars in OMC-1. The proper motion vector of SrcI has a PA $= 152° \pm 4°$. It appears to be misaligned by $9 \pm 4°$with the SrcI disk major axis (PA $= -37° \pm 0.°4$, as observed at 220–340 GHz; M. Wright et al. 2020). The SrcI major axis aligns with the BN proper motion ($323° \pm 2°$; L. F. Rodríguez et al. 2017), within 2°. This is expected, as in the BN–SrcI interaction, material in orbit around the stars experienced a torque that align their disks with the stellar proper motion vectors (J. Bally et al. 2020). The small misalignment of the SrcI disk is consistent with the hypothesis that the BN–I interaction shaped the disk rather than subsequent BHL accretion. Misalignment of the SrcI disk with its proper motion may produce the turbulent wake seen in SO emission. It is also possible that this misalignment is the product of source x and the current SrcI binary, or merger remnant, having separated after the initial SrcI disk formation and relaxation.

Since the outer radius of SrcI's disk is smaller than the gravitational radius, $r_G \sim GM/v_{\rm rot}^2 \sim 130$ au, it is likely that most of the SrcI disk has had to re-form since the dynamic interaction ∼550 yr ago from preexisting circumstellar material. This formation process may be contributing to the current accretion (and outflow). The fallback and resulting turbulence might contribute to shocks and enhanced accretion from disk to star.

Figure 10 shows the 215.221 GHz SO emission with uniform weighting of the $u-v$ data to emphasize the small-scale structure with a velocity resolution of 1 km s^{-1}.

The SO line shows an envelope of emission around the disk, with a steep gradient at the SE end of the disk, and an extended tail to the NW of the disk. There are also significant emission features at 0.″2–0.″4 to the NE and SW of the disk. The emission surrounding the disk is largely redshifted, consistent with the 0.″2 resolution spectra of SrcI plotted by R. L. Plambeck & M. C. H. Wright (2016), in which the sulfur-bearing species (CS, H_2S, SO, and SO_2) exhibit prominent blueshifted absorption profiles.

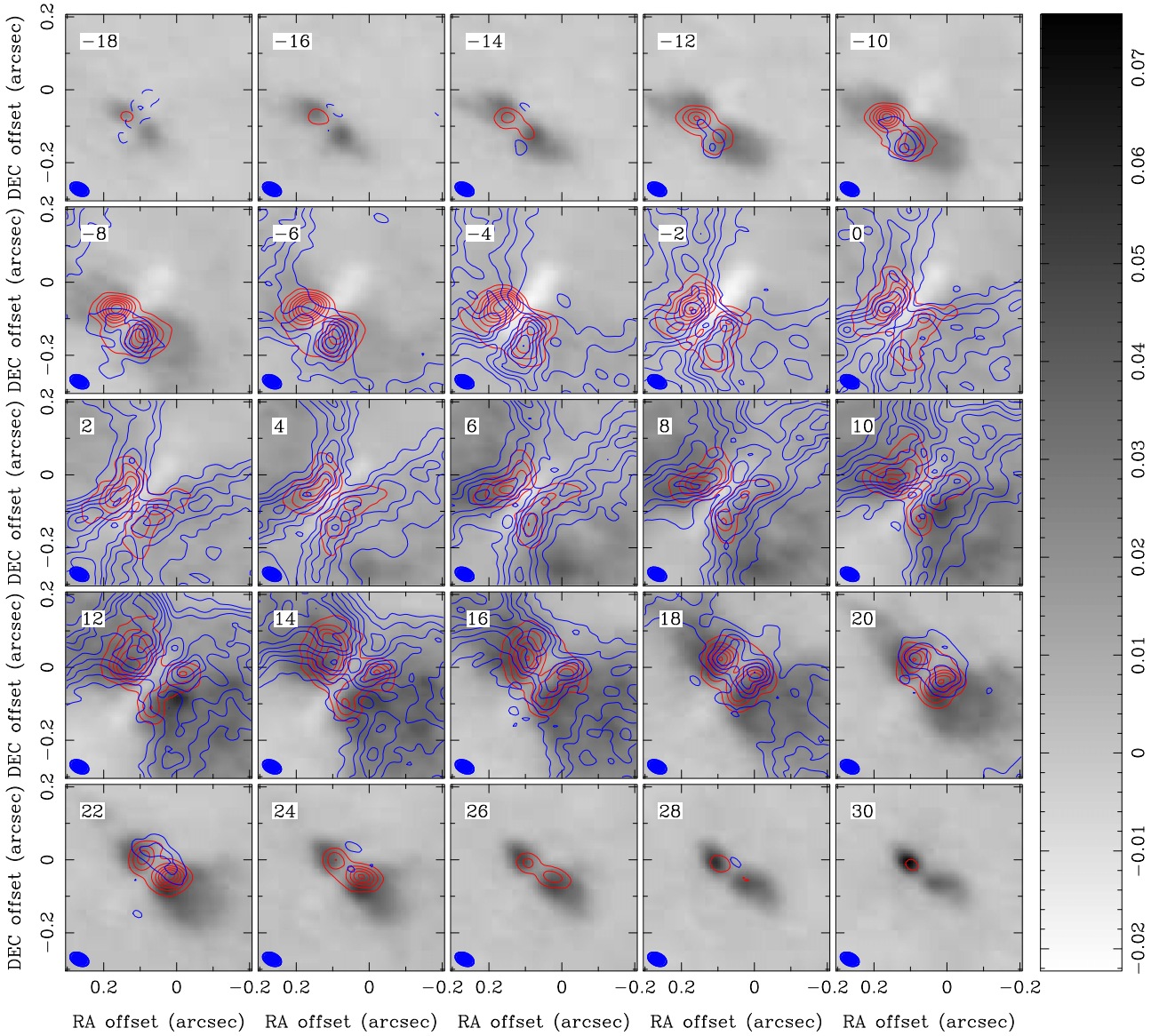

Figure 9. Structure and kinematics of H_2O, SiS, and SiO emission close to SrcI. This figure shows the 232.69 GHz H_2O emission (red contours), 217.82 GHz SiS emission (blue contours), and 217.10 GHz SiO $v = 0$ $J = 5$–4 (pixel image) in 2 km s^{-1} channels. The SiO emission is shown as the grayscale in units of Jy beam^{-1} as indicated in the wedge. The continuum emission from the disk has been subtracted from the images. The SiO emission is seen in absorption against the disk and is visible in white.

SO and SO_2 are heavily absorbed across SrcI at velocities of -8 to $+4$ km s^{-1} (M. Wright et al. 2020). This blueshifted absorption is the reason for the domination of redshifted emission around the disk. Since the velocity width of the absorption is comparable with the halfwidth of the SiO emission lines, it is likely that the absorbing molecules are located in the (cooler) outer layers of the SrcI outflow, rather than in unrelated foreground gas (R. L. Plambeck & M. C. H. Wright 2016).

In Figure 10, the 215.221 GHz SO $v = 0$ ($J = 5$–4) line shows a steep gradient at the SE end of the disk, with an extended tail to the NW of the disk. The SO suggests a bow shock from the motion of SrcI through the medium, with a turbulent wake similar to the simulations in N. Moeckel & H. B. Throop (2009). SO is heavily present in the region around the disk, and very roughly follows a velocity pattern around the disk. The leading (SE) side of the disk has blueshifted SO emission, while the leeward side has redshifted SO emission. This would be expected if SO was wrapping around the disk between the outflow lobes; about half the incoming SO would have a velocity component toward us along our line of sight to the disk, and redshifted toward the leeward side of SrcI.

Past this region, we see a significant body of SO extending away from the disk that has a small $v_{\rm los}$ component (indicated in green, where $0 < v_{\rm los} < 10$ km s^{-1}). Figure 11 shows the velocity structure of the trailing plume of 215.22 GHz SO emission to the NW of the disk, using natural weighting of the u–v data to enhance the brightness sensitivity in 1 km s^{-1} intervals. The rms noise level is 9 mJy beam^{-1} (35 K) in a synthesized beam FWHM 95×76 mas at PA $-83°$.

This region may correspond to the "quasi-static" body mentioned above. Material within a radius $R_A = 2GM/(c_s^2 + v^2) \sim 270$ au for $M \sim 15\,M_\odot$, will be accreted on a

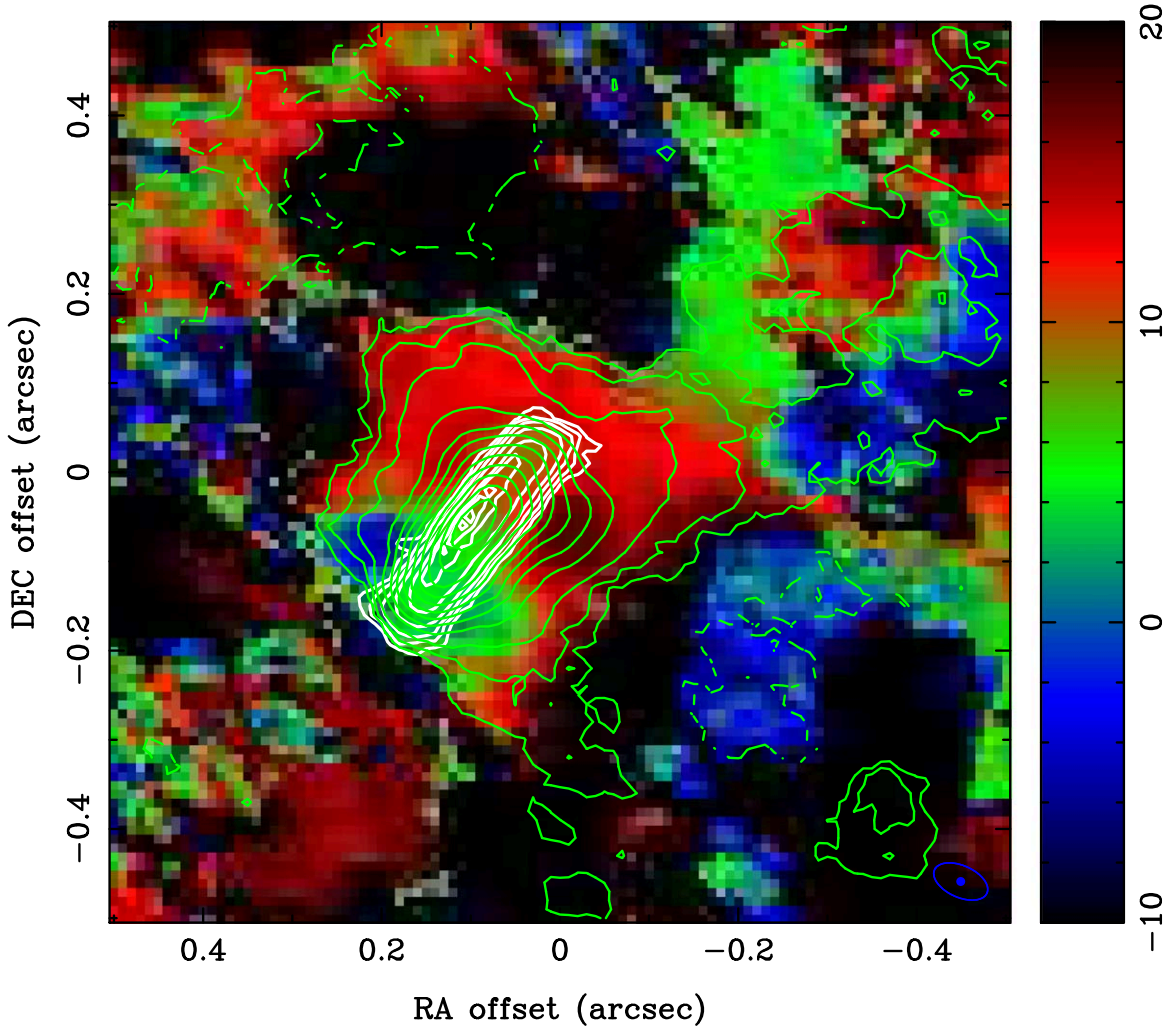

Figure 10. SO 215.22 GHz emission with uniform weighting of the $u-v$ data to emphasize the fine-scale structure. The color image shows the moment 1 velocity image with velocities from −10 to +20 km s^{-1} indicated in the color wedge. Green contours show the SO emission, integrated over a velocity range of −20 to +30 km s^{-1}. Contour levels are at −0.3, −0.2, −0.1, −0.05, 0.025, 0.05, 0.1, 0.2, 0.3, 0.4, 0.5, 0.6, 0.7, 0.8, 0.9, 1 Jy beam^{-1} × km s^{-1}. The peak brightness with 1 km s^{-1} velocity resolution is 744 K. The synthesized beam FWHM (64 × 36 mas, PA 66°) is indicated in blue in the lower right. The white contour map shows 340 GHz continuum emission at levels 25, 50, 100, 200, 400, 500, 600, 700, 800 K. The continuum image has been convolved by a 10 mas FWHM beam.

timescale $R_A/c_s \sim 1000$ yr (N. Moeckel & H. B. Throop 2009), where $c_s = \sqrt{k_B T/\mu m_p}$ is the ambient thermal (sound) speed ∼1.4 km s^{-1} for $T \sim 500$ K.

In addition, studies have shown using simulations that the radiation pressure exerted by massive protostars does not preclude accretion; mass can be delivered into the star through nonaxisymmetric disks and filaments that self-shield against radiation, created by gravitational and Rayleigh–Taylor instabilities while radiation escapes through optically thin bubbles (M. R. Krumholz et al. 2009). Gravitational instabilities can also lead to the formation of companion stellar objects (M. R. Krumholz et al. 2009).

Another difficulty of getting material to infall upon massive stars is removing the angular momentum from the accreting material. The accretion disk is a mediating structure for this process, providing a buffer between the surrounding material and the protostar. For further discussion of this topic, see R. E. Pudritz & T. P. Ray (2019).

The material accretes onto the disk as it loses some angular momentum, and then more angular momentum is removed through processes such as D-winds and X-winds (F. H. Shu et al. 2000), resulting in material falling onto the protostar from the disk. These steps are time-variable and may not always occur at the same rate relative to one another. X-winds are an alternative mechanism for generating outflows from disks. According to this model, high-velocity outflows come from a narrow annulus where the star magnetosphere interacts directly with the inner edge of the disk, at the corotation radius (F. H. Shu et al. 2000). The hot spot observed on the inner edge of the SrcI disk (A. Ginsburg et al. 2018) may result from this mechanism, or alternatively from the proximity of a binary protostar. If SrcI is a binary protostar, it is not clear how the magnetospheres of the two stars interact with each other, and with the disk.

Observations of the scattered near-infrared emission suggest that the near-infrared reflection spectrum observed in the Orion-KL region is produced close to SrcI, and similar to stellar photospheres in the range $T_{\rm eff} \sim 3500$ to 4500 K (L. Testi et al. 2010). The spectrum excludes SrcI being a massive protostar rotating at breakup speed. L. Testi et al. (2010) suggest that the absorption spectrum comes from a disk surrounding a $\sim 10\,M_\odot$ protostar, accreting from its disk at a high rate of a few $\times 10^{-3}\,M_\odot$ yr^{-1}.

T. Hosokawa et al. (2010) studied the evolution of massive protostars with disk accretion. They identified four evolutionary phases, including deuterium burning which may

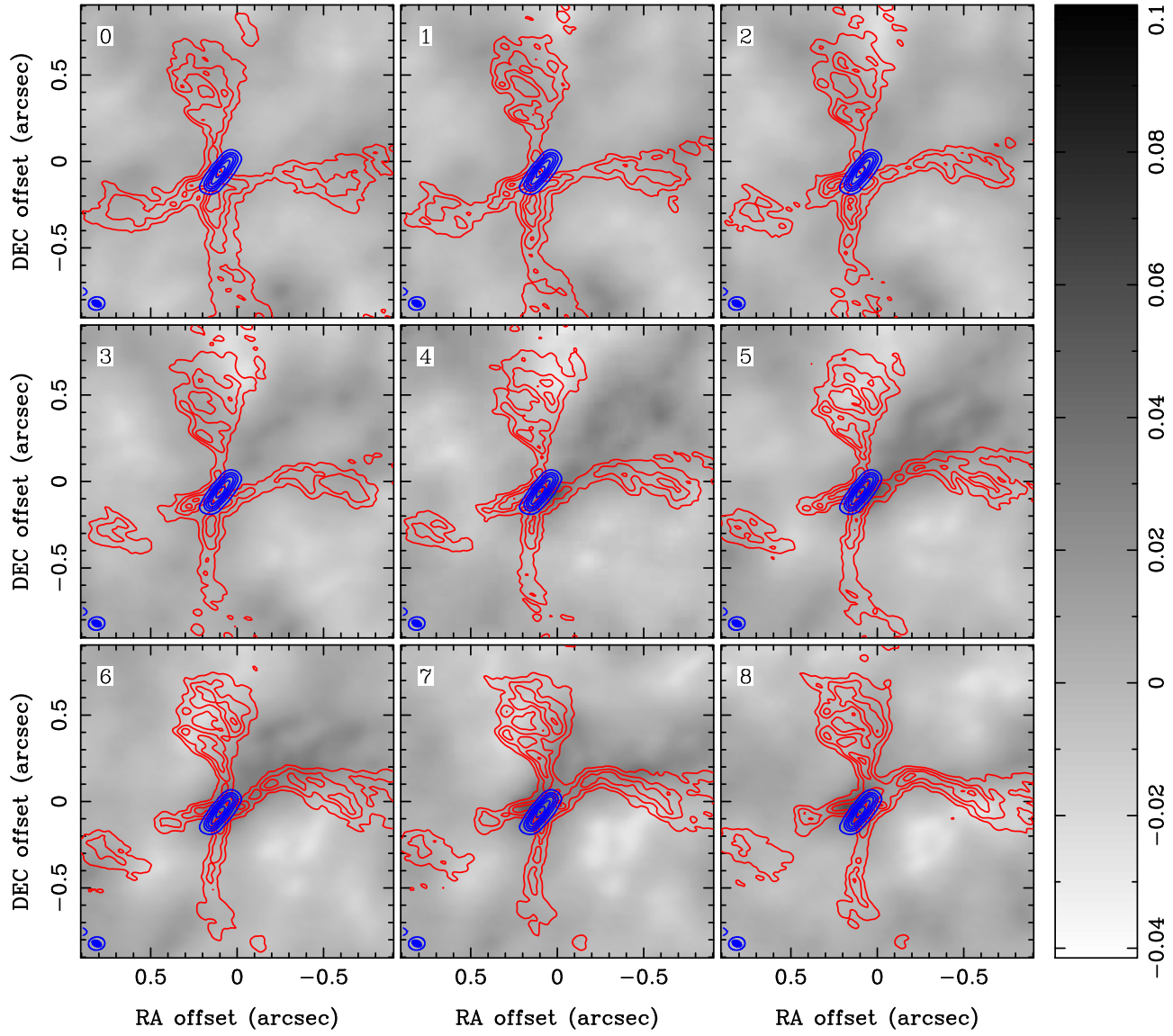

Figure 11. SO and SiS emission in 1 km s^{-1} channels. The gray pixel image shows the 215.22 GHz SO emission with channels in 1 km s^{-1} intervals. The u–v data were naturally weighted to enhance the brightness sensitivity. The wedge shows the SO brightness in units of Jy beam^{-1}. The rms noise = 9 mJy beam^{-1} (35 K). The synthesized beam FWHM (95 × 76 mas, PA −83°) is indicated by the blue outline in the lower left. The red contours map the 217.82 GHz SiS emission. Contour levels are at 5, 10, 15, 20, 25, 30, and 35 mJy beam^{-1}. The blue contours map the 218 GHz continuum emission from the SrcI disk. Contour levels are at 5, 10, 15, 20, 25, 30, and 35 mJy beam^{-1}. The synthesized beam FWHM (54 × 34 mas, PA 65°) is indicated in solid blue in the lower left.

account for a significant fraction of the luminosity of SrcI at some point. However, their models show that a massive protostar bloats to a radius of several hundreds of $R_\odot$ with an accretion rate exceeding $10^{-3}\,M_\odot\,\mathrm{yr}^{-1}$. The large radius leads to a low effective temperature consistent with that observed for SrcI. They also note that the low UV luminosity will inhibit the formation of an H II region until mass accretion onto the star decreases significantly. Assuming a stellar radius of 1 au with color temperature 4000 K, the theoretical luminosity would be,

$$L_{\rm tot} = 4\pi R^2 \sigma T^4 \simeq 1.01 \times 10^4 L_\odot.$$

Comparatively, if we assume an infall rate $5 \times 10^{-3}\,M_\odot\,\mathrm{yr}^{-1}$ onto a central mass of $15\,M_\odot$, the luminosity to be

$$L_{\rm tot} = \frac{GM\dot{M}}{R} \simeq 1.05 \times 10^4 L_\odot.$$

Currently, no direct observations of infall onto SrcI have been made. The expected infall rate ($\dot{M}$) is inferred from the observed outflow to range from 10^{-5} to $10^{-3}\,M_\odot\,\mathrm{yr}^{-1}$. The H_2O rotation fitting done by A. Ginsburg et al. (2018) favors a $\sim 15\,M_\odot$ protostar with a high accretion rate.

To maintain the observed luminosity of $\sim 10^4\,L_\odot$, if the accretion onto the circumbinary disk is akin to the Bondi–Hoyle rate ($\sim 10^{-7}\,M_\odot\,\mathrm{yr}^{-1}$) and accretion from the disk onto the star is $\sim 10^{-3}\,M_\odot\,\mathrm{yr}^{-1}$, then the disk will be depleted on a timescale of $M_{\rm disk}/\dot{M}$. R. L. Plambeck & M. C. H. Wright (2016) estimated $M_{\rm disk} \sim 0.02$ to $0.2 M_\odot$, giving a disk depletion time of 200–2000 yr for $\dot{M} \sim 10^{-3}\,M_\odot\,\mathrm{yr}^{-1}$.

If a higher rate of accretion onto the circumbinary disk is not occurring, then the protostar will likely deplete the disk and reach the final stage of its pre-main-sequence evolution. This is a rather exciting possibility, as it would expect SrcI to become a directly visible stellar object within several centuries. However, the source would still be in the Orion A cloud for a while. To emerge into the Orion Nebula would take tens of thousands of years. If it is currently ∼0.1 pc behind the

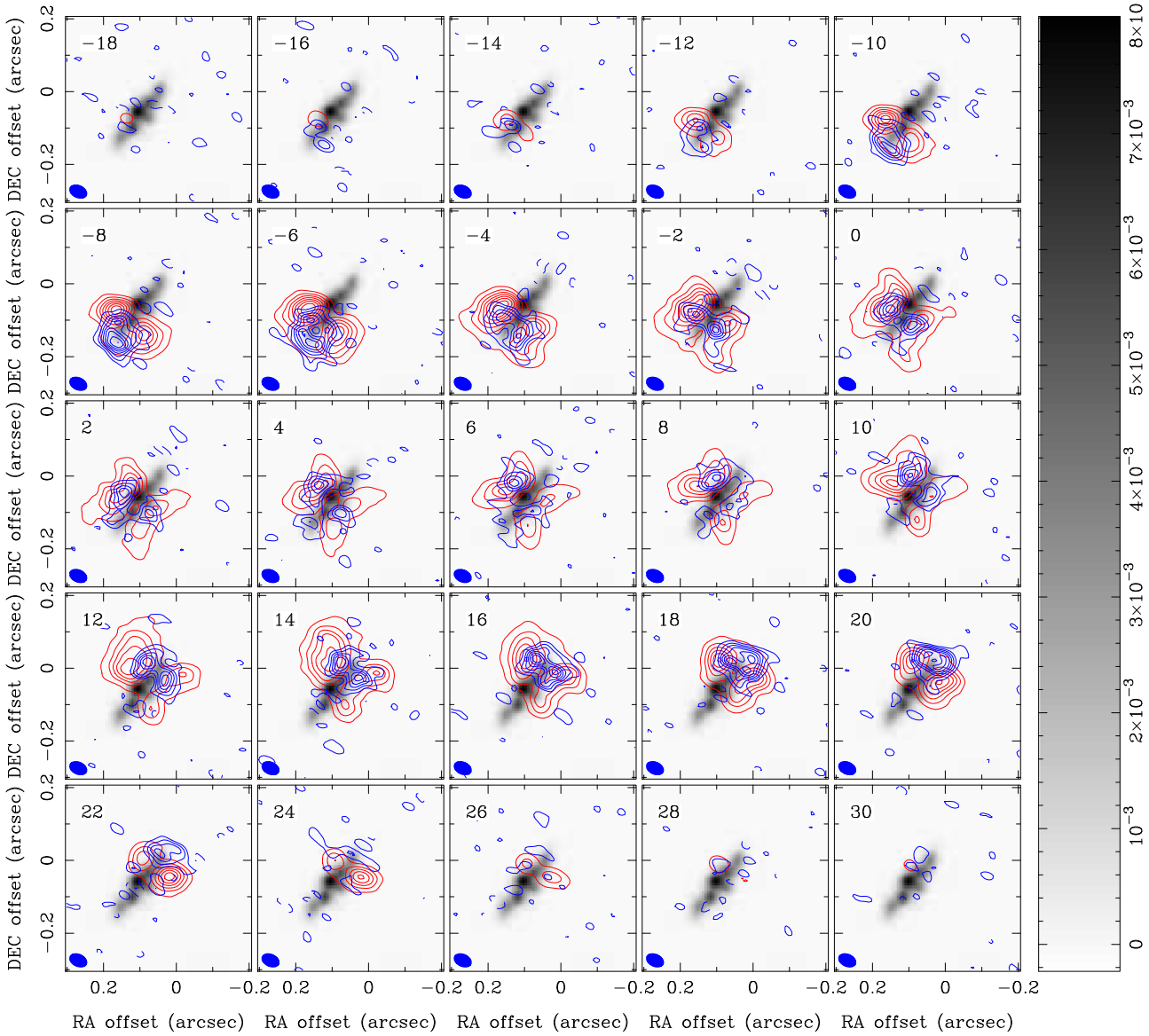

Figure 12. H_2O and NaCl emission in 2 km s^{-1} channels. Comparison of the 232.69 GHz H_2O emission (red contours) and the 232.51 GHz NaCl emission (blue contours). Both NaCl and H_2O map the rotation of the disk. The NaCl emission is more closely associated with the continuum disk and extends to greater radii along the disk major axis than the H_2O emission. The synthesized beam FWHM for the H_2O and NaCl (54 × 34 mas, PA 66°) is indicated in blue in the lower left. The 99 GHz continuum emission is shown as the gray pixel image with brightness from 0 to 9 mJy beam^{-1} indicated in the wedge. The continuum data have been convolved by a 30 mas FWHM beam.

ionization front with a radial velocity $(v_r) \sim 4$ km s^{-1}, this would take $\sim 2.5 \times 10^4$ yr. Also, if $\dot{M} \sim 10^{-3}\, M_\odot$ yr^{-1}, the photosphere will remain on the astronomical unit scale, and after the disk is gone, it will take a Kelvin–Helmholtz timescale to heat up from 4000 to ∼40,000 K for the newborn star to begin ionizing the surroundings.

4.6. Evidence of a Warped Disk in Salt Emission

Salt emission has been detected in nine high-mass young stellar object (YSO) disks so far A. Ginsburg et al. (2019, 2023), L. T. Maud et al. (2019), and K. E. I. Tanaka et al. (2020). In SrcI, salt emission is found close to the dust layer at the surface of SrcI and maps the rotation close to the disk surface (A. Ginsburg et al. 2018, 2019).

A comparison of the H_2O and NaCl at $\sim 50 \times 30$ mas resolution is shown in Figure 12. The NaCl emission is more closely associated with the continuum disk and extends to greater radii along the disk major axis than the H_2O emission. Figure 4 shows the moment 1 image—the velocity-weighted intensity—of the NaCl emission. This shows a simple, linear velocity gradient (implied by the linear color gradient across the disk), which is consistent with an almost edge-on thick disk. L. D. Matthews et al. (2010) found that the SiO masers suggest an inclination of ∼85°. Additionally, A. Ginsburg et al. (2018) fitted a Keplerian rotation curve to the envelope of a position–velocity along the major axis of the SrcI disk in good agreement.

Using a linear velocity gradient combined with the observed NaCl moment 0 image, we generated model images in 2 km s^{-1} channels for comparison with the data shown in Figure 13.

This simple model agrees with the observed NaCl emission in 2 km s^{-1} channels between −10 and +20 km s^{-1}. The maximum differences between the model and the data occur at the ends of the disk where the model and the data are

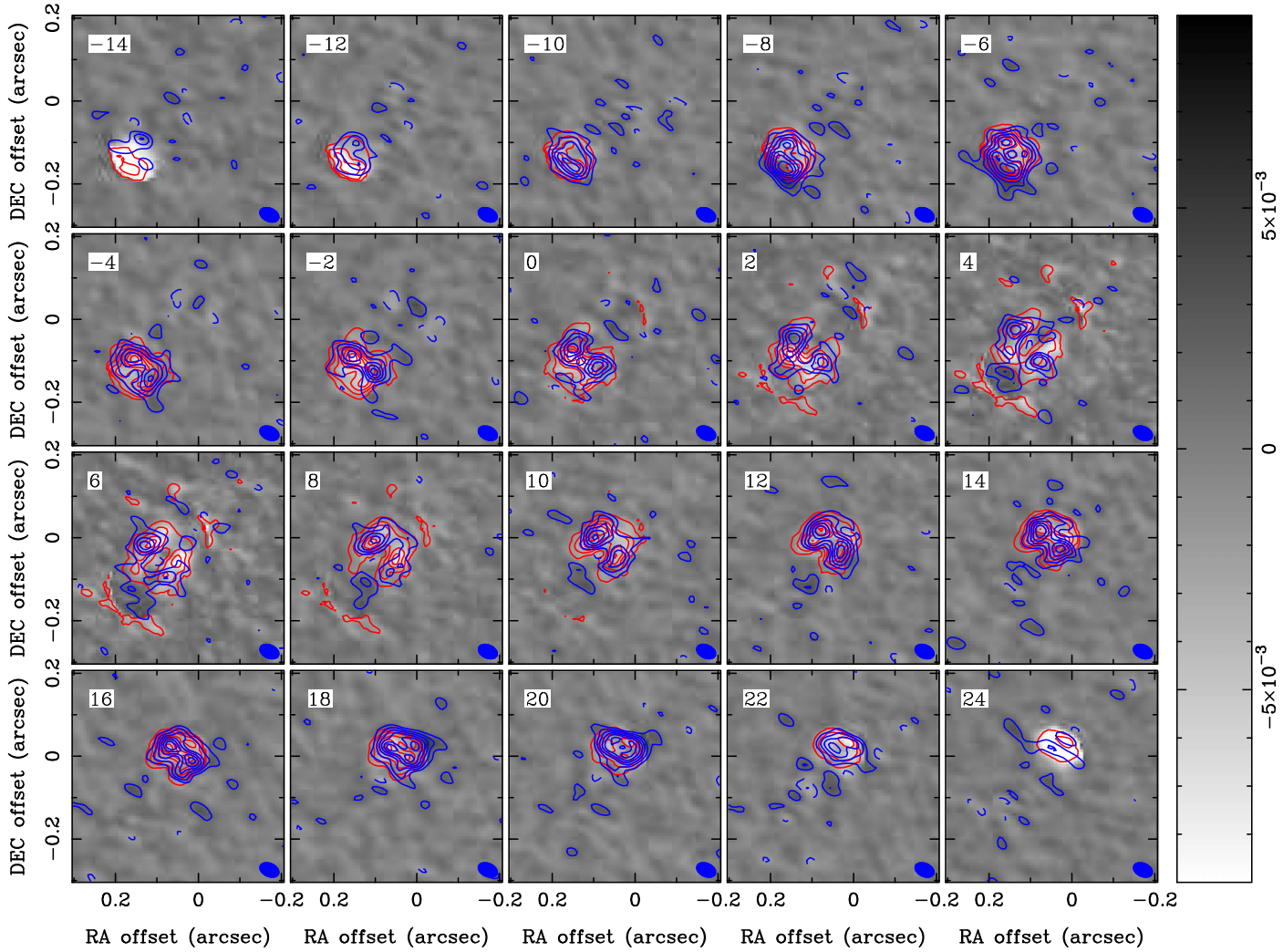

Figure 13. Structure and kinematics of NaCl emission. Comparison of the structure and kinematics of the observed NaCl emission and a model generated from a linear velocity gradient along the disk major axis. The blue contours show the 232.51 GHz NaCl emission in 2 km s^{-1} channels. Contour levels are at −32, −16, 16, 32, 48, 64, 80, 96, 112, and 128 mJ beam^{-1}. The red contours show the simulated emission from a model rotation curve. The gray pixel image shows the difference between the model and the data in units of Jy beam^{-1} indicated in the wedge. Note the significant difference between the data and the model at large absolute velocities. The rms error of this image is 1.2 mJy beam^{-1}. The synthesized beam FWHM (47 × 31 mas, PA 65°) is indicated in blue in the lower right.

asymmetrically offset. We used the MIRIAD tool imdiff to fit the offset as as a function of the velocity. The offsets can be minimized by allowing the position angle of the disk to change with radius. A possible explanation for this disagreement at the velocity and radial extrema is that the NaCl emission resulted from (recently) accreted material having a different angular momentum compared to the original disk, which resulted from the BN/SrcI encounter. Accreted material, or the localized outflow resulting from accreted material, could exert a torque. This may produce the warping observed in the 99 GHz continuum emission from the disk (M. Wright et al. 2022) and the NaCl emission at the ends of the disk. Alternatively, misalignment between the rotation axis and the B-field direction could also create a warped disk structure (M. N. Machida et al. 2020).

Additionally, the salt lines could be excited by the infall of material onto the disk. Figure 14 shows a comparison of the 232.51 GHz NaCl $v = 1$ ($J = 18$–17) and the 217.98 GHz NaCl $v = 2$ ($J = 17$–16) in 2 km s^{-1} channels. Note that the $v = 1$ and $v = 2$ emission come from the same regions, and have the same velocity distribution, suggesting a common origin for different transitions. This common origin may be excitation due to shocks created by accretion onto the disk.

Figure 15 shows a comparison of 217.98 GHz NaCl $v = 2$ ($J = 17$–16) and SiO in 2 km s^{-1} channels. Note that the NaCl emission that comes from the ends of the disk may be a byproduct of an accretion shock of material falling into the disk, while the SiO emerges from a smaller radius in the disk, corresponding to the footprint of a magneto-centrifugal outflow from the disk. Some of the material falling toward the disk at radii within this footprint would be swept out by the outflow.

The symmetry of the NaCl bright spots about the rotation axis may be from the rotation of the disk. If this explanation is correct, then this implies that accretion is followed by orbital redistribution, i.e., the salt must stay in the gas phase for the orbital timescale at ∼30 au radius for a 15 $M_\odot$ star, >40 yr.

The vibrationally excited NaCl must be populated on these timescales because of the high Einstein A-values (A. Ginsburg et al. 2019). However, the density and temperature rise within 100–1000 yr as the shock goes through the surface layers of the disk (A. M. Burkhardt et al. 2019). The $1/e$ scale height of the disk surface estimated from the 340 GHz continuum is only a

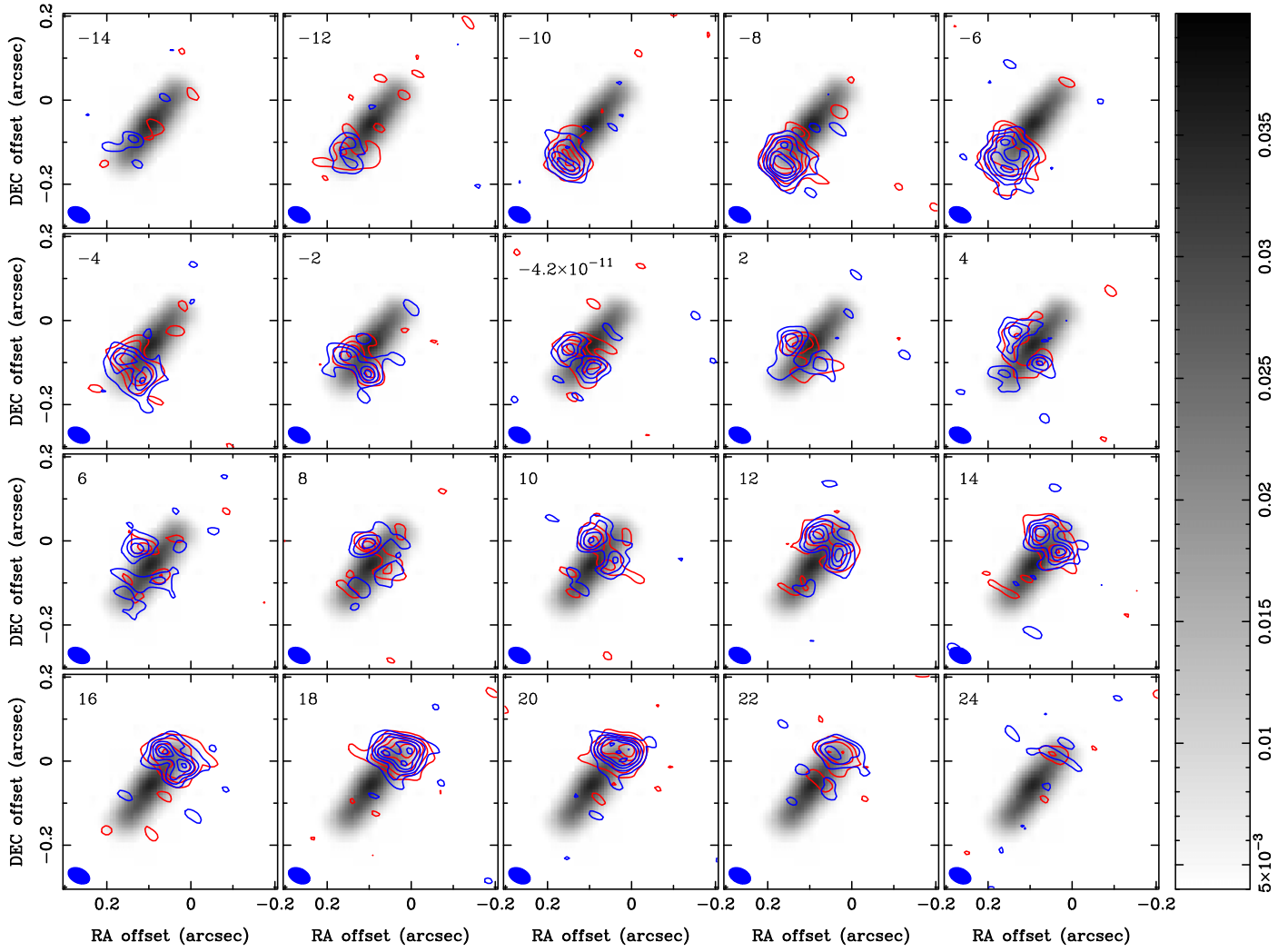

Figure 14. Comparison of two NaCl emission lines. A comparison of the 232.51 GHz NaCl $v = 1$ $J = 18$–17 (blue contours) and the 217.98 GHz NaCl $v = 2$ $J = 17$–16 (red contours) in 2 km s^{-1} channels. Note that the $v = 1$ and $v = 2$ emission comes from the same regions in the disk at every velocity. Contours at 2, 4, 6, 8, and 10 mJy beam^{-1}. The pixel image shows the continuum emission from the disk at 230 GHz in units of Jy beam^{-1} indicated in the wedge. The synthesized beam FWHM is indicated in blue in the lower left.

few astronomical units (M. Wright et al. 2020) and presents a wide range of temperatures and densities for accreting material. More detailed modeling is needed to see if accretion shocks could populate the observed NaCl levels.

Similar to the NaCl distribution, observations of the $5_0 - 4_0$ (A) methanol line at 241.79143 GHz, (E_u 35 K) in the surface layer at the ends of the disk in the Class 0 protostellar object L1157 have been previously reported as evidence for an accretion shock (T. Velusamy et al. 2002).

A. Ginsburg et al. (2023) took a sample of 23 candidate high-mass YSOs (HMYSOs) in 17 high-mass star-forming regions and found five new detections of H_2O, NaCl, KCl, PN, and SiS. While these detections had disk-like kinematic structures, SrcI is the only HMYSO that has been confirmed to have these molecules present in its disk. These results indicate that NaCl emission features are likely common in HMYSO disks.

5. Summary

1. We present ALMA observations of SiO, SiS, H_2O, NaCl, and SO at ∼30–50 mas resolution. These images map the molecular outflow and disk of Orion Source I (SrcI) on ∼12–20 au scales.
2. The SiO and ^{29}SiO emission map a rotating, expanding outflow. The emission is consistent with a magneto-centrifugal outflow from the SrcI disk. The rotational velocity decreases with distance from the disk.
3. The SiS maps a turbulent boundary layer in the outflow. We argue that the SiS emission is created and destroyed in a shocked region between the outflow and the ambient medium as SrcI moves through it. This process would dissipate the angular momentum held by the rotating molecular outflow into the surrounding medium.
4. The vibrationally excited water line (E_u = 3461.9 K) traces the rotation of the SrcI disk and also traces the SiO outflow and SiS emission close to the disk, suggesting that shocks may play a role in the H_2O emission. The origin of the vibrationally excited water line in the gas phase is not clear. The H_2O emission extends deeper and likely formed in the disk, but icy grain mantles could not persist in the hot disk. Hydrated minerals are a possible source of H_2O in the hot disk.

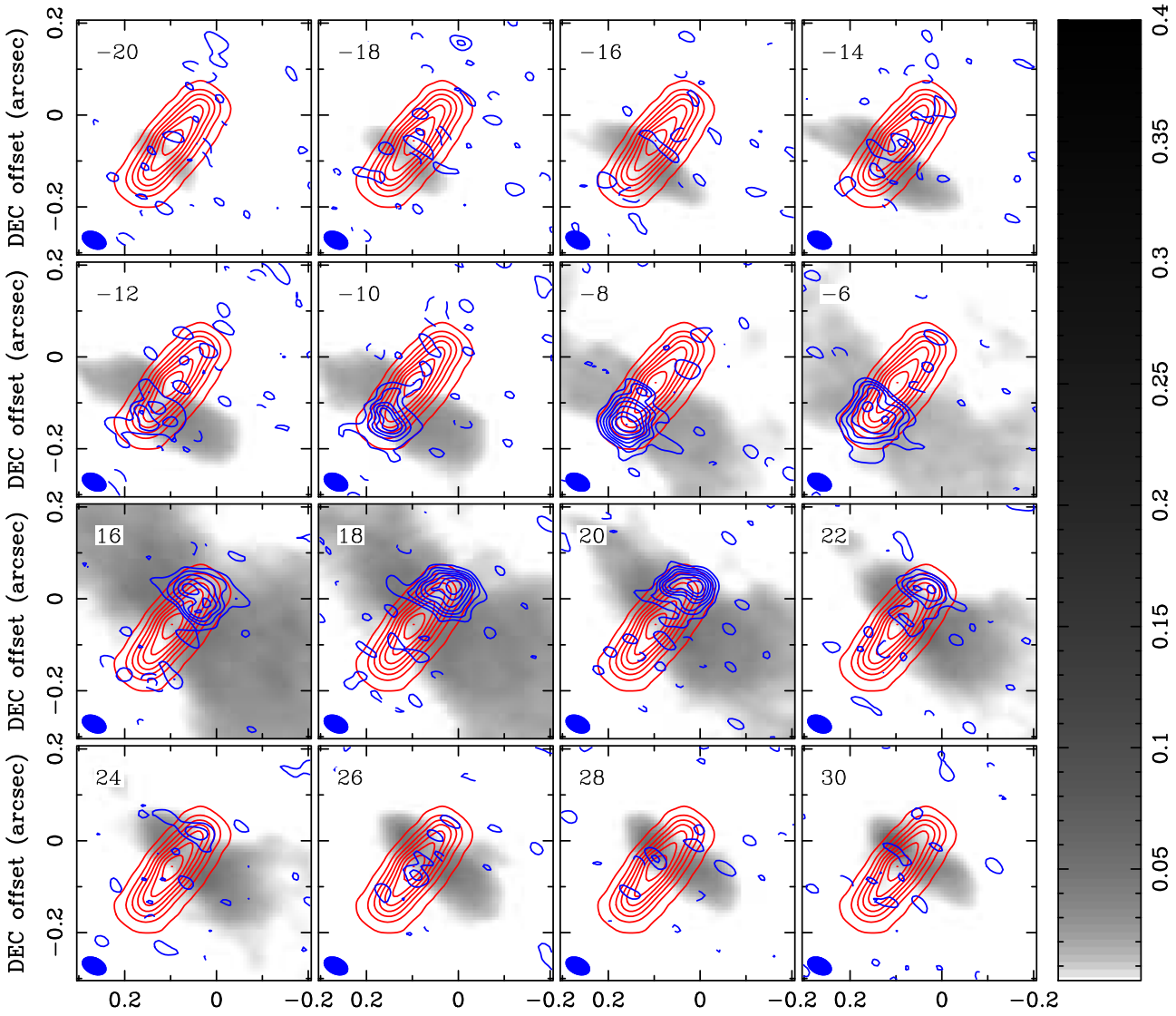

Figure 15. NaCl and SiO outflow. Comparison of NaCl $v = 2$ 17–16 at 217.98 GHz (blue contours at intervals 1.46 mJy beam^{-1}) and SiO in 2 km s^{-1} channels shown in the grayscale image in units Jy beam^{-1} on a log scale from 0.04 to 0.4 Jy beam^{-1} as indicated in the wedge. Note the NaCl emission at the ends of the disk, while the SiO has footprints at a smaller radius in the disk. The 217 GHz continuum emission is shown in red contours at intervals 4.36 mJy beam^{-1}. The synthesized beam FWHM is indicated in blue in the lower left.

5. The NaCl emission closely traces the disk. The emission follows a linear velocity gradient along the disk's major axis. At both ends of the disk, the position angle of the NaCl emission is consistent with a twist, or warp. Bright hot spots in NaCl emission may be excited by accretion shocks from material falling onto the disk. The motion of SrcI forces the external material to pass between the disk and the outflow, which may result in some material accreting onto the disk, creating shocks that excite the NaCl emission close to the disk surface.
6. SO traces a bow shock at the leading edge of the SrcI disk and a turbulent plume of material extending from the trailing edge of the disk. This trailing material may accrete onto the disk. These features are created by the movement of SrcI through the medium and BHL accretion.
7. If the accretion onto the circumbinary disk is the BHL rate $\sim 10^{-7}\,M_{\odot}\,\mathrm{yr}^{-1}$ and accretion from the disk onto the star is $\sim 10^{-3}\,M_{\odot}\,\mathrm{yr}^{-1}$ to maintain the observed luminosity of $\sim 10^{4}\,L_{\odot}$, then the disk is being depleted on a timescale time of 200–2000 yr.
8. These data suggest that the BN–SrcI interaction, and the proper motion of SrcI may have a significant effect on the structure and evolution of SrcI and its molecular outflow.

Acknowledgments

We thank the referee for a careful review and detailed suggestions to improve this paper.

The National Radio Astronomy Observatory is a facility of the National Science Foundation operated under a cooperative agreement by Associated Universities, Inc. This paper makes use of the following ALMA data: 2017.1.00497.S, 2016.1.00165.S, 2016.1.00165.S. ALMA is a partnership of ESO (representing its member states), NSF (USA) and NINS (Japan), together with NRC (Canada), MOST and ASIAA (Taiwan), and KASI (Republic of Korea), in cooperation with the Republic of Chile. The Joint ALMA Observatory is operated by ESO, AUI/NRAO

and NAOJ. T.H. is financially supported by the MEXT/JSPS KAKENHI grant Nos. 17K05398, 18H05222, and 20H05845. A.G. acknowledges support from the NSF under AAG 2008101 and CAREER 2142300. J.B. acknowledges support from NSF grants AST1910393 and AST2206513.

Facilities: ALMA, VLA.

Software: Miriad (R. J. Sault et al. 1995).

ORCID iDs

Brett A. McGuire https://orcid.org/0000-0003-1254-4817
Adam Ginsburg https://orcid.org/0000-0001-6431-9633

References

Bally, J., Ginsburg, A., Arce, H., et al. 2017, ApJ, 837, 60
Bally, J., Ginsburg, A., Forbrich, J., & Vargas-González, J. 2020, ApJ, 889, 178
Bonnell, I. A. 2008, in ASP Conf. Ser. 390, Pathways Through an Eclectic Universe, ed. J. H. Knapen, T. J. Mahoney, & A. Vazdekis (San Francisco, CA: ASP), 26
Bonnell, I. A., Bate, M. R., & Zinnecker, H. 1998, MNRAS, 298, 93
Burkhardt, A. M., Shingledecker, C. N., Gal, R. L., et al. 2019, ApJ, 881, 32
Campanha, D. R., Mendoza, E., Silva, M. X., et al. 2022, MNRAS, 515, 369
Caratti o Garatti, A., Stecklum, B., Garcia Lopez, R., et al. 2017, NatPh, 13, 276
Charnley, S. B. 1997, ApJ, 481, 396
Commerçon, B., González, M., Mignon-Risse, R., Hennebelle, P., & Vaytet, N. 2022, A&A, 658, A52
Doddipatla, S., He, C., Goettl, S. J., et al. 2021, SciA, 7, eabg7003
Dzib, S. A., Loinard, L., Rodríguez, L. F., et al. 2017, ApJ, 834, 139
Edgar, R. 2004, NewAR, 48, 843
Ginsburg, A., Bally, J., Goddi, C., Plambeck, R., & Wright, M. 2018, ApJ, 860, 119
Ginsburg, A., McGuire, B., Plambeck, R., et al. 2019, ApJ, 872, 54
Ginsburg, A., McGuire, B. A., Sanhueza, P., et al. 2023, ApJ, 942, 66
Goddi, C., Greenhill, L. J., Chandler, C. J., et al. 2009, ApJ, 698, 1165
Goddi, C., Greenhill, L. J., Humphreys, E. M. L., Chandler, C. J., & Matthews, L. D. 2011a, ApJL, 739, L13
Goddi, C., Humphreys, E. M. L., Greenhill, L. J., Chandler, C. J., & Matthews, L. D. 2011b, ApJ, 728, 15
Greenhill, L. J., Goddi, C., Chandler, C. J., Matthews, L. D., & Humphreys, E. M. L. 2013, ApJL, 770, L32
Hirota, T., Kim, M. K., Kurono, Y., & Honma, M. 2014, ApJL, 782, L28
Hirota, T., Machida, M. N., Matsushita, Y., et al. 2017, NatAs, 1, 0146
Hirota, T., Plambeck, R. L., Wright, M. C. H., et al. 2020, ApJ, 896, 157
Hosokawa, T., Yorke, H. W., & Omukai, K. 2010, ApJ, 721, 478
Indriolo, N., Neufeld, D. A., Seifahrt, A., & Richter, M. J. 2013, ApJ, 776, 8
Kim, M. K., Hirota, T., Honma, M., et al. 2008, PASJ, 60, 991
Kounkel, M., Covey, K., Suárez, G., et al. 2018, AJ, 156, 84
Krumholz, M. R., Klein, R. I., McKee, C. F., Offner, S. S. R., & Cunningham, A. J. 2009, Sci, 323, 754
Kuiper, R., Klahr, H., Beuther, H., & Henning, T. 2011, ApJ, 732, 20
Lenzuni, P., Gail, H.-P., & Henning, T. 1995, ApJ, 447, 848
Li, J., Wang, J., Zhu, Q., Zhang, J., & Li, D. 2015, ApJ, 802, 40
López-Vázquez, J. A., Zapata, L. A., Lizano, S., & Cantó, J. 2020, ApJ, 904, 158
Luhman, K. L., Robberto, M., Tan, J. C., et al. 2017, ApJL, 838, L3
Machida, M. N., Hirano, S., & Kitta, H. 2020, MNRAS, 491, 2180
Matthews, L. D., Greenhill, L. J., Goddi, C., et al. 2010, ApJ, 708, 80
Maud, L. T., Cesaroni, R., Kumar, M. S. N., et al. 2019, A&A, 627, L6
Menten, K. M., Reid, M. J., Forbrich, J., & Brunthaler, A. 2007, A&A, 474, 515
Minh, Y. C., Ziurys, L. M., Irvine, W. M., & McGonagle, D. 1990, ApJ, 360, 136
Moeckel, N., & Throop, H. B. 2009, ApJ, 707, 268
Neufeld, D. A., Falgarone, E., Gerin, M., et al. 2012, A&A, 542, L6
Niederhofer, F., Humphreys, E. M. L., & Goddi, C. 2012, A&A, 548, A69
Paiva, M. A. M., Lefloch, B., & Galvão, B. R. L. 2020, MNRAS, 493, 299
Pillich, C., Bogdan, T., Landers, J., Wurm, G., & Wende, H. 2021, A&A, 652, A106
Pineau des Forets, G., Roueff, E., Schilke, P., & Flower, D. R. 1993, MNRAS, 262, 915
Plambeck, R. L., & Wright, M. C. H. 2016, ApJ, 833, 219
Plambeck, R. L., Wright, M. C. H., Friedel, D. N., et al. 2009, ApJL, 704, L25
Pudritz, R. E., & Ray, T. P. 2019, FrASS, 6, 54
Reid, M. J., Menten, K. M., Greenhill, L. J., & Chandler, C. J. 2007, ApJ, 664, 950
Rodríguez, L. F., Dzib, S. A., Loinard, L., et al. 2017, ApJ, 834, 140
Rodríguez, L. F., Dzib, S. A., Zapata, L., et al. 2020, ApJ, 892, 82
Rosi, M., Mancini, L., Skouteris, D., et al. 2018, CPL, 695, 87
Sault, R. J., Teuben, P. J., & Wright, M. C. H. 1995, in ASP Conf. Ser. 77, Astronomical Data Analysis Software and Systems IV, ed. R. A. Shaw, H. E. Payne, & J. J. E. Hayes (San Francisco, CA: ASP), 433
Schilke, P., Benford, D. J., Hunter, T. R., Lis, D. C., & Phillips, T. G. 2001, ApJS, 132, 281
Schilke, P., Walmsley, C. M., Pineau des Forets, G., & Flower, D. R. 1997, A&A, 321, 293
Shu, F. 1991, The Physics of Astrophysics: Gas Dynamics (Mill Valley, CA: Univ. Science Books)
Shu, F. H., Najita, J. R., Shang, H., & Li, Z.-Y. 2000, Protostars and Planets IV (Tucson, AZ: Univ. Arizona Press), 789
Snell, R. L., Scoville, N. Z., Sanders, D. B., & Erickson, N. R. 1984, ApJ, 284, 176
Tanaka, K. E. I., Zhang, Y., Hirota, T., et al. 2020, ApJL, 900, L2
Testi, L., Tan, J. C., & Palla, F. 2010, A&A, 522, A44
Ulrich, R. K. 1976, ApJ, 210, 377
van der Tak, F. F. S., Walmsley, C. M., Herpin, F., & Ceccarelli, C. 2006, A&A, 447, 1011
van Dishoeck, E. F., & Blake, G. A. 1998, ARA&A, 36, 317
van Gelder, M. L., Tabone, B., van Dishoeck, E. F., & Godard, B. 2021, A&A, 653, A159
Velusamy, T., Langer, W. D., & Goldsmith, P. F. 2002, ApJL, 565, L43
Wakelam, V., Ceccarelli, C., Castets, A., et al. 2005, A&A, 437, 149
Wakelam, V., Hersant, F., & Herpin, F. 2011, A&A, 529, A112
Whitney, B. A., Robitaille, T. P., Bjorkman, J. E., et al. 2013, ApJS, 207, 30
Wright, M., Bally, J., Hirota, T., et al. 2022, ApJ, 924, 107
Wright, M., Plambeck, R., Hirota, T., et al. 2020, ApJ, 889, 155